JM PAPERS

Capillary flow of evaporating liquid solutions in open rectangular microchannels

Panayiotis Kolliopoulos[1], Krystopher S. Jochem[1], Lorraine F. Francis[1] and Satish Kumar[1],†

[1]Department of Chemical Engineering and Materials Science, University of Minnesota, Minneapolis, MN 55455, USA

Capillary flow of liquids plays a key role in many applications including lab-on-a-chip devices, heat pipes and printed electronics manufacturing. Open rectangular microchannels often appear in these applications, with the lack of a top resulting in a complex free-surface morphology and evaporation. In this work we develop a theoretical model based on lubrication theory and kinetically limited evaporation to examine capillary flow of evaporating liquid solutions in open rectangular microchannels connected to circular reservoirs. The model accounts for the complex free-surface morphology, solvent evaporation, Marangoni flows due to gradients in solute concentration and temperature and finite-size reservoir effects. Significant differences are predicted in flow behaviour between pure liquids and liquid solutions due to solvent evaporation and solute transport. Marangoni flows are found to promote more uniform solute deposition patterns after solvent evaporation. Model predictions of meniscus position evolution are in good agreement with prior capillary-flow experiments of aqueous poly(vinyl alcohol) solutions in the presence of evaporation. The model reveals that the principal mechanism through which evaporation influences the meniscus position in the experiments is the increase in viscosity with solute concentration.

Key words: microfluidics, condensation/evaporation, capillary flows

1. Introduction

Spontaneous capillary-driven imbibition of liquids into microchannels plays a central role in applications such as lab-on-a-chip devices (Olanrewaju *et al.* 2018; Narayanamurthy *et al.* 2020), heat pipes (Faghri 1995, 2012), evaporative lithography (Lone *et al.* 2017) and fabrication of flexible printed electronics (Lone *et al.* 2017; Cao *et al.* 2018; Jochem *et al.* 2018, 2020). These applications use either closed or open microchannels. A closed

† Email address for correspondence: kumar030@umn.edu

microchannel is defined as one where all walls are solid whereas an open microchannel lacks a top.

Early studies by Lucas (1918) and Washburn (1921) proposed theoretical models describing the time evolution of the meniscus position $\hat{z}_M$, where flow is driven by capillary-pressure gradients caused by a circular-arc meniscus front. For horizontal capillary tubes, an analytical solution $\hat{z}_M = \sqrt{\hat{k}\hat{t}}$ is obtained, commonly referred to as the Lucas–Washburn relation, where the mobility parameter $\hat{k}$ can be thought of as a diffusion coefficient driving the growth of the liquid interface. Multiple studies extended the work of Lucas (1918) and Washburn (1921) by accounting for inertial (Rideal 1922; Bosanquet 1923; Quéré 1997), dynamic contact angle (Siebold *et al.* 2000; Popescu, Ralston & Sedev 2008; Ouali *et al.* 2013) and surface roughness (Ouali *et al.* 2013; Xing, Cheng & Zhou 2020) effects, and generalized the Lucas–Washburn relation to arbitrary cross-sectional geometries (Ouali *et al.* 2013; Berthier, Gosselin & Berthier 2015). Comparison of model predictions with experiments (Yang *et al.* 2011; Ouali *et al.* 2013; Chen 2014; Sowers *et al.* 2016; Kolliopoulos *et al.* 2019; Liu *et al.* 2021) confirms the $\hat{z}_M \sim \hat{t}^{1/2}$ relationship.

Due to advancements in lithographic fabrication techniques and micromoulding, open microchannels with various cross-sectional geometries can be fabricated easily and inexpensively, including rectangular (Yang *et al.* 2011; Sowers *et al.* 2016; Lade *et al.* 2018; Kolliopoulos *et al.* 2019, 2021), trapezoidal (Chen 2014), U-shaped (Yang *et al.* 2011) and V-shaped (Mann *et al.* 1995; Rye, Mann & Yost 1996; Yost, Rye & Mann 1997; Rye, Yost & O'Toole 1998) cross-sections. However, the mechanism for flow in open channels is more complex than for closed channels because the additional free surface due to the lack of a top wall also drives the flow (Romero & Yost 1996; Weislogel & Lichter 1998; Weislogel 2012; Gurumurthy *et al.* 2018; White & Troian 2019; Kolliopoulos *et al.* 2021).

In addition to this complex free-surface morphology, the lack of a top allows evaporation to significantly affect flow if the liquid is volatile. In applications such as microfluidic devices used for diagnostic testing, evaporation can undesirably influence test results. In contrast, in applications such as flexible printed electronics fabrication via the self-aligned capillarity-assisted lithography for electronics (SCALE) process, evaporation is exploited to print conductive inks on flexible substrates which can be integrated with roll-to-roll manufacturing processes, resulting in low-cost and high-throughput device fabrication (Mahajan *et al.* 2015; Cao *et al.* 2018; Jochem *et al.* 2018, 2020).

Motivated by heat-pipe applications, previous studies have considered the effects of evaporation on steady flow in rectangular (Nilson *et al.* 2006; Xia, Yang & Wang 2019) and V-shaped (Khrustalev & Faghri 1994; Peterson & Ma 1996; Suman & Hoda 2005; Markos, Ajaev & Homsy 2006) channels. Gambaryan-Roisman (2019) recently examined the influence of diffusion-limited evaporation on capillary-flow dynamics in V-shaped channels. However, these previous studies focus on pure liquids, whereas many applications rely on capillary flow of liquid solutions or colloidal suspensions.

One of the first studies to investigate the effects of evaporation on capillary flow in open rectangular microchannels was conducted by Lade *et al.* (2018). This study was motivated by the SCALE process (Mahajan *et al.* 2015; Cao *et al.* 2018; Jochem *et al.* 2018, 2020), which uses evaporation during capillary flow for the fabrication of flexible printed electronics. Uniform deposition of solute suspended in the evaporating liquid is generally required for the electronic devices to function well. The length of travel down a channel and the size of the liquid reservoir feeding the channel are also critical to the design of SCALE circuits. Lade *et al.* (2018) conducted experiments using polymer solutions and the rate of evaporation was controlled using a humidity chamber.

Kolliopoulos *et al.* (2019) extended the Lucas–Washburn model by including the effects of concentration-dependent viscosity and uniform evaporation, and compared model predictions with the experiments of Lade *et al.* (2018). Their model, however, did not account for solute concentration gradients and used the evaporation rate $\hat{J}$ as a fitting parameter. While scaling relationships obtained from this model for the dependence of the final flow time ($\hat{t} \sim 1/\hat{J}$) and final liquid-front position ($\hat{z}_M \sim 1/\hat{J}^{1/2}$) on the rate of evaporation were in good agreement with the experimental observations, there was an $O(10 - 10^2)$ discrepancy between the evaporation rates used to fit the model and the estimates obtained from experiments. This discrepancy was attributed to not accounting for the complex free-surface morphology and the spatial concentration gradients due to solute accumulation at the contact line. Kolliopoulos *et al.* (2019) also assumed an infinite supply of liquid into the channel and did not account for effects from the finite-size reservoir used in the experiments of Lade *et al.* (2018).

In this work we develop a lubrication-theory-based model (§§ 2 and 3) to study capillary flow of evaporating liquid solutions in open rectangular microchannels. The model accounts for the complex free-surface morphology, solvent evaporation, Marangoni flows due to gradients in solute concentration and temperature and finite-size reservoir effects. We initially consider the effect of channel aspect ratio and equilibrium contact angle on the temperature and evaporative mass flux profiles (§ 4.1). We isolate thermal effects by considering a pure solvent (§ 4.2) and investigate solute-concentration effects in a liquid solution (§ 5). Then, model predictions are compared with the capillary-flow experiments of Lade *et al.* (2018) (§ 6), followed by concluding remarks (§ 7).

2. Mathematical model

We consider an incompressible Newtonian liquid solution in an open rectangular channel in contact with an ambient gas phase. The liquid consists of a volatile solvent and a non-volatile solute. We assume the solvent and solute densities are equal such that the liquid has a constant density $\hat{\rho}$. The liquid has viscosity $\hat{\mu}$ and surface tension $\hat{\sigma}$, which are dependent on the solute concentration c (mass fraction) and liquid temperature $\hat{T}$. It is assumed that the liquid has a constant equilibrium contact angle θ_0 with the channel walls. Evaporation of the solvent is induced by increasing the temperature of the channel walls $\hat{T}_W$ or by decreasing the relative humidity R_H of the ambient gas phase. We assume the liquid thermal conductivity $\hat{k}$ and heat capacity $\hat{C}_p$ are constant. In this work, we use the notation $\hat{f}$ to denote the dimensional version of a variable f.

2.1. *Model geometry*

An open rectangular channel with width $\hat{W}$, height $\hat{H}$ and length $\hat{L}$, connected to a reservoir of radius $\hat{R}$ is depicted in figure 1. The amount of liquid in the reservoir is described using the contact angle on the reservoir sidewall θ_R. The contact line is assumed to be pinned to the top of the reservoir sidewall. As described in Kolliopoulos *et al.* (2021), the free surface undergoes a transition from that observed in figure 1(*a*) ($\lambda \geq \lambda_c$) to that in figure 1(*b*) ($\lambda < \lambda_c$). Here, $\lambda = \hat{H}/\hat{W}$ is the channel aspect ratio and $\lambda_c = (1 - \sin \theta_0)/2 \cos \theta_0$ is the aspect ratio at which the circular upper meniscus contacts the bottom of the rectangular channel while being attached to the top of the channel sidewalls with an equilibrium contact angle θ_0.

Each regime is described using the liquid height $\hat{a}$ and the contact angle θ on the channel sidewall. For $\lambda \geq \lambda_c$ (figure 1*a*), the free-surface morphology is divided into three regimes along the channel length: meniscus deformation $[0, \hat{z}_D]$, meniscus recession $[\hat{z}_D, \hat{z}_M]$ and
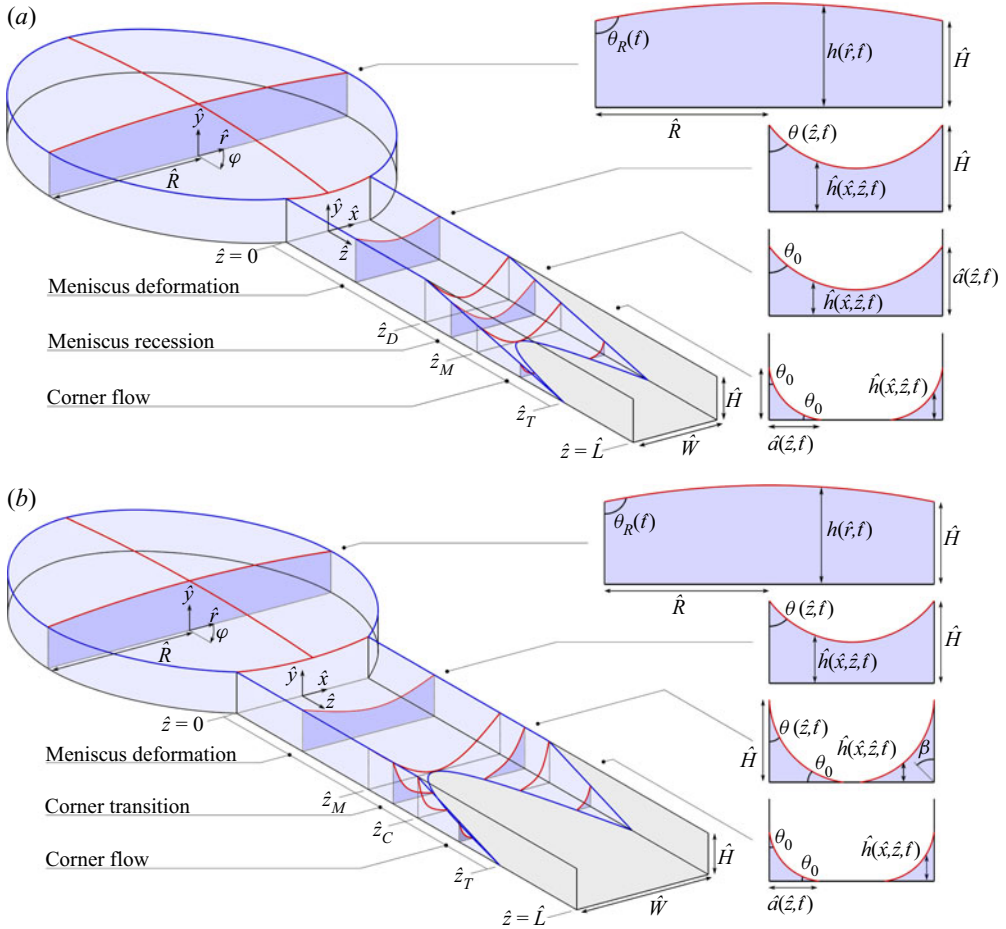
Figure 1. Schematic of liquid undergoing capillary flow in an open rectangular channel connected to a circular reservoir for aspect ratios (a) $\lambda \geq \lambda_c$ and (b) $\lambda < \lambda_c$. Here, $\beta = \arctan(\cos\theta / \cos\theta_0)$ and the finger length is $\tilde{z}_T - \tilde{z}_M$.

corner flow $[\hat{z}_M, \hat{z}_T]$. In the meniscus-deformation regime, the upper meniscus curvature at the channel inlet is matched to the liquid–air interface curvature in the reservoir and the upper meniscus curvature increases down the channel length until $\theta(\hat{z}_D, \hat{t}) = \theta_0$, while the liquid remains pinned to the top of the channel sidewall $\hat{a} = \hat{H}$.

In the meniscus-recession regime, the contact angle on the sidewall remains constant at $\theta = \theta_0$ and the liquid height recedes down the sidewall until the upper meniscus contacts the channel bottom $\hat{a}(\hat{z}_M, \hat{t}) = \hat{W}\lambda_c$. At this point, the contact angle on the bottom is assumed to reach θ_0 instantaneously. This is the simplest possible assumption, implies a neglect of contact-angle hysteresis, and works well in describing experiments in the absence of evaporation (Kolliopoulos *et al.* 2021). Subsequently, the flow splits into the channel corners, leading to the corner-flow regime. Here, the contact angle on the sidewall and bottom remains constant at $\theta = \theta_0$ and the liquid height further recedes down the sidewall from $\hat{a}(\hat{z}_M, \hat{t}) = \hat{W}\lambda_c$ to $\hat{a}(\hat{z}_T, \hat{t}) = 0$ at the finger tip.

938 A22-4

For $\lambda < \lambda_c$ (figure 1b) the free-surface morphology is also divided into three regimes: meniscus deformation $[0, \hat{z}_M]$, corner transition $[\hat{z}_M, \hat{z}_C]$ and corner flow $[\hat{z}_C, \hat{z}_T]$. In the meniscus-deformation regime, the liquid is pinned to the top of the sidewall ($\hat{a} = \hat{H}$). The upper meniscus curvature at the channel inlet is matched to the liquid–air interface curvature in the reservoir and the upper meniscus curvature increases down the channel length until $\theta(\hat{z}_M, \hat{t}) = \theta_C$ when the upper meniscus touches the channel bottom.

Upon contact with the channel bottom, the contact angle there is assumed to reach θ_0 instantaneously. The upper meniscus splits into the channel corners, yielding the corner-transition regime. During this stage, the liquid remains pinned to the top of the sidewall ($\hat{a} = \hat{H}$). To conserve mass, the contact angle at the sidewall $\theta(\hat{z}_M, \hat{t})$ must change from θ_C to another value denoted θ_T. The contact angle on the sidewall decreases down the channel length until $\theta(\hat{z}_C, \hat{t}) = \theta_0$, at which point the flow transitions to the corner-flow regime. Here, $\theta = \theta_0$ and the liquid depins from the top of the sidewall and decreases until $\hat{a}(\hat{z}_T, \hat{t}) = 0$.

In the following sections we develop a mathematical model for capillary flow of a liquid solution with evaporation considering both $\lambda \geq \lambda_c$ (figure 1a) and $\lambda < \lambda_c$ (figure 1b), and account for the finite-size reservoir used in experiments (Lade *et al.* 2018).

2.2. *Hydrodynamics*

Mass and momentum conservation for an incompressible Newtonian liquid are governed by

$$\widehat{\nabla} \cdot \hat{\boldsymbol{u}} = 0 \quad \text{and} \quad \hat{\rho}\left[\frac{\partial \hat{\boldsymbol{u}}}{\partial \hat{t}} + (\hat{\boldsymbol{u}} \cdot \widehat{\nabla})\hat{\boldsymbol{u}}\right] = -\widehat{\nabla}\hat{p} + \hat{\mu}\widehat{\nabla}^2\hat{\boldsymbol{u}} + \hat{\rho}\hat{\boldsymbol{g}}, \qquad (2.1a)$$

where $\hat{\boldsymbol{u}} = (\hat{u}, \hat{v}, \hat{w})$ is the velocity in Cartesian coordinates $(\hat{x}, \hat{y}, \hat{z})$, $\hat{p}$ is the liquid pressure and $\hat{\boldsymbol{g}} = (\hat{g}_x, \hat{g}_y, \hat{g}_z)$ is the gravitational acceleration. Along the channel walls, the no-slip and no-penetration conditions require $\hat{\boldsymbol{u}} = 0$. The boundary conditions for the jump in normal, transverse tangential, and axial tangential stresses across the liquid–air interface $\hat{h}(\hat{x}, \hat{z}, \hat{t})$ are

$$[\![\boldsymbol{n} \cdot \hat{\boldsymbol{T}} \cdot \boldsymbol{n}]\!] = \hat{\sigma}(\widehat{\nabla}_s \cdot \boldsymbol{n}), \quad [\![\boldsymbol{t}_1 \cdot \hat{\boldsymbol{T}} \cdot \boldsymbol{n}]\!] = \boldsymbol{t}_1 \cdot \widehat{\nabla}_s\hat{\sigma}, \quad \text{and} \quad [\![\boldsymbol{t}_2 \cdot \hat{\boldsymbol{T}} \cdot \boldsymbol{n}]\!] = \boldsymbol{t}_2 \cdot \widehat{\nabla}_s\hat{\sigma}. \qquad (2.1b)$$

Here, $\hat{\boldsymbol{T}} = -\hat{p}\boldsymbol{I} + \hat{\mu}[\widehat{\nabla}\hat{\boldsymbol{u}} + (\widehat{\nabla}\hat{\boldsymbol{u}})^{\mathrm{T}}]$ is the stress tensor, $\boldsymbol{I}$ is the identity tensor, $\widehat{\nabla}_s = \widehat{\nabla} - \boldsymbol{n}(\boldsymbol{n} \cdot \widehat{\nabla})$ is the surface-gradient operator, $\boldsymbol{n}$ is the unit outward normal vector and $\boldsymbol{t}_1$, $\boldsymbol{t}_2$ are the two unit tangent vectors to the interface in the transverse and axial directions, respectively. These vectors are given by

$$\boldsymbol{n} = \frac{(-\hat{h}_{\hat{x}}, 1, -\hat{h}_{\hat{z}})}{\sqrt{1 + \hat{h}_{\hat{x}}^2 + \hat{h}_{\hat{z}}^2}}, \quad \boldsymbol{t}_1 = \frac{(1 + \hat{h}_{\hat{z}}^2, \hat{h}_{\hat{x}}, -\hat{h}_{\hat{x}}\hat{h}_{\hat{z}})}{\sqrt{(1 + \hat{h}_{\hat{z}}^2)^2 + \hat{h}_{\hat{x}}^2 + \hat{h}_{\hat{x}}^2\hat{h}_{\hat{z}}^2}}, \quad \boldsymbol{t}_2 = \frac{(0, \hat{h}_{\hat{z}}, 1)}{\sqrt{1 + \hat{h}_{\hat{z}}^2}}. \qquad (2.2a\text{--}c)$$

Equations (2.1a) are rendered dimensionless using the following scalings:

$$\left.\begin{array}{l} (\hat{x}, \hat{y}, \hat{z}) = \hat{L}(\epsilon x, \epsilon y, z), \quad (\hat{u}, \hat{v}, \hat{w}) = \hat{U}(\epsilon u, \epsilon v, w), \quad (\hat{g}_x, \hat{g}_y, \hat{g}_z) = \hat{g}(g_x, g_y, g_z), \\[4pt] \hat{t} = (\hat{L}/\hat{U})t, \quad \epsilon = \hat{H}/\hat{L}, \quad \hat{U} = \epsilon\hat{\sigma}_0/\hat{\mu}_0, \quad \hat{p} = (\hat{\mu}_0\hat{U}/\epsilon\hat{H})p, \quad \hat{\mu} = \hat{\mu}_0 M, \quad \hat{\sigma} = \hat{\sigma}_0\Sigma, \end{array}\right\} \qquad (2.3)$$

where ϵ is the 'slenderness' parameter, $\hat{U}$ is the viscocapillary velocity, $\hat{\mu}_0$ is the solvent viscosity, $\hat{\sigma}_0$ is the solvent surface tension and M and Σ are the dimensionless solution

viscosity and surface tension, respectively, defined in §2.6. The dimensionless numbers that arise are the Reynolds number $Re = \hat{\rho}\hat{U}\hat{H}/\hat{\mu}_0$ (ratio of inertial to viscous forces), the capillary number $Ca = \hat{\mu}_0\hat{U}/\epsilon\hat{\sigma}_0$ (ratio of viscous to surface-tension forces) and the Bond number $Bo = \hat{\rho}\hat{g}\hat{H}^2/\hat{\sigma}_0$ (ratio of gravitational to surface-tension forces). Note that $Ca = 1$ based on our choice of $\hat{U}$.

In the limits where $\epsilon^2 \ll 1$, $\epsilon Re \ll 1$ and $Bo/Ca \ll \epsilon$, (2.1a) reduces to

$$u_x + v_y + w_z = 0, \tag{2.4a}$$

$$p_x = p_y = 0, \tag{2.4b}$$

$$p_z = M(w_{xx} + w_{yy}). \tag{2.4c}$$

The boundary conditions at the free surface in (2.1b) reduce to

$$p - p_{V,T} = -\frac{\Sigma}{Ca}\left[\frac{h_x}{(1+h_x^2)^{1/2}}\right]_x = -\frac{\Sigma}{Ca}\kappa, \tag{2.5a}$$

$$(1 - h_x^2)(v_x + u_y) + 2h_x(-u_x + v_y) - (1 - h_x^2)h_z w_x - 2h_x h_z w_y$$
$$= -h_x h_z (1 + h_x^2)^{1/2}\frac{\Sigma_z}{MCa}, \tag{2.5b}$$

$$w_y - h_x w_x = \frac{\Sigma_z}{MCa}, \tag{2.5c}$$

where $p_{V,T}$ is the total pressure in the vapour phase and is assumed constant. Since the leading-order pressure term is independent of (x, y) according to (2.4b), the leading-order curvature term κ only depends on (z, t) according to (2.5a).

We note two things about these reduced equations. First, the interface shape at a given z-position is determined by capillary statics (Yang & Homsy 2006), as can be seen from (2.5a). As a consequence, contact angles can be imposed as boundary conditions without having to specify a slip law. The interface shape slowly varies in the z-direction via an evolution equation to be presented in §2.7. This approach is expected to hold for $\hat{\mu}_0\hat{U}/\hat{\sigma}_0 \ll 1$. Second, because of the problem we are considering and our choice of variables, h_x is $O(1)$, so the h_x^2 terms are retained.

As shown by Kolliopoulos *et al.* (2021), using a condition for the contact-line location on the solid wall, a symmetry condition, and the definition of the contact angle on the sidewall, expressions for $p(z, t)$ and $h(x, z, t)$ are obtained by integrating (2.5a) twice with respect to x, leading to

meniscus deformation
$$\begin{cases} p = -2\Sigma\lambda\cos\theta(z,t) + p_{V,T}, \\ h = 1 + \dfrac{\tan\theta(z,t)}{2\lambda} - \left[\dfrac{1}{4\lambda^2\cos^2\theta(z,t)} - x^2\right]^{1/2}, \\ A = \dfrac{1}{4\lambda^2}\left[4\lambda - \dfrac{\pi/2 - \theta(z,t)}{\cos^2\theta(z,t)} + \tan\theta(z,t)\right], \end{cases} \tag{2.6a}$$

meniscus recession
$$\begin{cases} p = -2\Sigma\lambda\cos\theta_0 + p_{V,T}, \\ h = a(z,t) + \dfrac{\tan\theta_0}{2\lambda} - \left[\dfrac{1}{4\lambda^2\cos^2\theta_0} - x^2\right]^{1/2}, \\ A = \dfrac{1}{4\lambda^2}\left[4\lambda a(z,t) - \dfrac{\pi/2 - \theta_0}{\cos^2\theta_0} + \tan\theta_0\right], \end{cases} \tag{2.6b}$$

$$\text{corner transition} \quad \begin{cases} p = -\Sigma[\cos\theta_0 - \sin\theta(z,t)] + p_{V,T}, \\ h = \dfrac{\cos\theta\cos\beta}{\cos(\theta+\beta)} - \left[\left(\dfrac{\sin\beta}{\cos(\theta+\beta)}\right)^2 - \left(\dfrac{\cos\theta\sin\beta}{\cos(\theta+\beta)} - x - \dfrac{1}{2\lambda}\right)^2\right]^{1/2}, \\ A = \dfrac{B(\theta,\theta_0)}{(\cos\theta_0 - \sin\theta)^2}, \end{cases}$$

$$(2.6c)$$

$$\text{corner flow} \quad \begin{cases} p = -\dfrac{\Sigma[\cos\theta_0 - \sin\theta_0]}{a(z,t)} + p_{V,T}, \\ h = \dfrac{a\cos\theta_0\cos\frac{\pi}{4}}{\cos(\theta_0+\frac{\pi}{4})} - \left[\left(\dfrac{a\sin\frac{\pi}{4}}{\cos(\theta_0+\frac{\pi}{4})}\right)^2 - \left(\dfrac{a\cos\theta_0\sin\frac{\pi}{4}}{\cos(\theta_0+\frac{\pi}{4})} - x - \dfrac{1}{2\lambda}\right)^2\right]^{1/2}, \\ A = \dfrac{a^2 B(\theta_0,\theta_0)}{(\cos\theta_0 - \sin\theta_0)^2}, \end{cases}$$

$$(2.6d)$$

where $\beta = \arctan(\cos\theta/\cos\theta_0)$ and $A = 2\int_{x_1}^{x_2} h\,\mathrm{d}x$ is the dimensionless liquid cross-sectional area. Note that θ and a in (2.6) are dependent on (z,t). The integration bounds for each regime are

$$\left.\begin{array}{l} \text{meniscus deformation:} \quad x_1 = 0 \quad \text{and} \quad x_2 = \dfrac{1}{2\lambda}, \\[2mm] \text{meniscus recession:} \quad x_1 = 0 \quad \text{and} \quad x_2 = \dfrac{1}{2\lambda}, \\[2mm] \text{corner transition:} \quad x_1 = \dfrac{1}{2\lambda} - \dfrac{\cos\theta - \sin\theta_0}{\cos\theta_0 - \sin\theta} \quad \text{and} \quad x_2 = \dfrac{1}{2\lambda}, \\[2mm] \text{corner flow:} \quad x_1 = \dfrac{1}{2\lambda} - a\dfrac{\cos\theta - \sin\theta_0}{\cos\theta_0 - \sin\theta} \quad \text{and} \quad x_2 = \dfrac{1}{2\lambda}. \end{array}\right\}$$

$$(2.7)$$

The geometric function $B(\theta,\theta_0)$ in the expressions for A is given by

$$B(\theta,\theta_0) = \theta + \theta_0 - \pi/2 - \cos\theta(\sin\theta - \cos\theta_0) + \cos\theta_0(\cos\theta - \sin\theta_0). \qquad (2.8)$$

Equations (2.6) were also used by Kolliopoulos *et al.* (2021) and in other previous studies (Romero & Yost 1996; Weislogel & Lichter 1998; Tchikanda, Nilson & Griffiths 2004; Weislogel & Nardin 2005; Nilson *et al.* 2006; Yang & Homsy 2006; White & Troian 2019).

2.3. *Evaporation*

We assume the liquid is in contact with a gas phase having ambient temperature $\hat{T}_A$ and relative humidity R_H. The gas phase consists of saturated vapour or a mixture of solvent vapour and inert gas (e.g. air), and its velocity is assumed to be negligible. We assume the gas phase density $\hat{\rho}_V$, viscosity $\hat{\mu}_V$, and thermal conductivity $\hat{k}_V$, are much smaller than their liquid counterparts (Burelbach, Bankoff & Davis 1988), and the temperature across the liquid–air interface is continuous (Sefiane & Ward 2007). These assumptions allow us to describe evaporation using a kinetically limited model focusing only on the liquid phase.

A kinetically limited model is chosen instead of a diffusion-limited model (Gambaryan-Roisman 2019) for three reasons. First, a kinetically limited model is expected to be more accurate at describing evaporating flow of liquid solutions since the presence of solute at the free surface

makes the rate-limiting step more likely to be in the liquid phase (Cazabat & Guéna 2010). Second, kinetically limited models have proven useful in interpreting experiments involving evaporation into an unsaturated environment when the vapour diffuses rapidly away from the evaporating interface even though they were originally developed for evaporation into a saturated environment (Murisic & Kondic 2011). Third, a kinetically limited model does not require keeping track of the solvent concentration in the vapour phase, which makes it computationally simpler while still providing qualitatively accurate predictions (Ajaev 2005; Murisic & Kondic 2011). We note that, although a kinetically limited model is expected to provide qualitatively accurate predictions, it is unlikely to produce quantitatively accurate predictions for situations where evaporation is diffusion limited.

Evaporation is modelled using the non-equilibrium Hertz–Knudsen relation based on the kinetic theory of gases (Plesset & Prosperetti 1976; Moosman & Homsy 1980). The evaporative mass flux is described using

$$\hat{j} = \alpha_E \hat{p}_V \left(\frac{\hat{R}_g \hat{T}|_{\hat{h}}}{2\pi} \right)^{1/2} \left(\frac{\hat{p}_{V,e}}{\hat{p}_V} - 1 \right), \tag{2.9}$$

where α_E is the thermal accommodation coefficient, $\hat{R}_g$ is the gas constant per unit mass, $\hat{T}|_{\hat{h}}$ is the local liquid–air interface temperature, $\hat{p}_V$ is the partial pressure of solvent in the vapour phase and $\hat{p}_{V,e}$ is the equilibrium solvent vapour pressure. Note that we have assumed the thermal accommodation coefficients for evaporation and condensation are equal to α_E. Physically, α_E can be thought of as a barrier to phase change, with $\alpha_E = 1$ corresponding to no barrier and $\alpha_E = 0$ corresponding to no phase change (Persad & Ward 2016). Prior studies have reported values of α_E that vary over several orders of magnitude from $O(10^{-6})$ to $O(1)$ (Marek & Straub 2001; Murisic & Kondic 2011). In this work, we use the accommodation coefficient as a fitting parameter when comparing with experiments, similar to Murisic & Kondic (2011).

According to equilibrium thermodynamics (Moosman & Homsy 1980; Ajaev & Homsy 2001; Ajaev 2005) we can write

$$\ln\left(\frac{\hat{p}_{V,e}}{\hat{p}_V} \right) = \frac{\hat{\mathcal{L}}}{\hat{R}_g} \left(\frac{1}{\hat{T}_V} - \frac{1}{\hat{T}|_{\hat{h}}} \right) + \frac{\hat{p} - \hat{p}_V}{\hat{\rho} \hat{R}_g \hat{T}|_{\hat{h}}}, \tag{2.10}$$

where $\hat{\mathcal{L}}$ is the latent heat and $\hat{T}_V$ is the vapour temperature. The partial pressure of solvent in the vapour phase is calculated using $\hat{p}_V = R_H \hat{p}_S(\hat{T}_A)$ (Cazabat & Guéna 2010; Murisic & Kondic 2011), where R_H is the relative humidity, which ranges from 0 to 1, and $\hat{p}_S(\hat{T}_A)$ is the saturation pressure corresponding to the ambient temperature $\hat{T}_A$. Both $\hat{p}_V$ and $\hat{T}_A$ in the vapour phase are assumed uniform and constant. The partial pressure of the solvent $\hat{p}_V$ is then used to calculate the vapour temperature $\hat{T}_V$ using the Clausius–Clapeyron equation (Murisic & Kondic 2011). Note that for $R_H = 1$ (which corresponds to a vapour phase saturated with solvent), $\hat{p}_V = \hat{p}_S$ and $\hat{T}_V = \hat{T}_A$.

We rescale (2.10) and (2.9) using

$$\hat{p} = (\hat{\mu}_0 \hat{U} / \epsilon \hat{H}) p, \quad \hat{T} = \hat{T}_V + T \Delta \hat{T}, \quad \Delta \hat{T} = \hat{T}_W - \hat{T}_V, \quad \text{and} \quad \hat{j} = (\hat{k} \Delta \hat{T} / \hat{\mathcal{L}} \hat{H}) j, \tag{2.11a–d}$$

where $\hat{T}_W$ is the temperature of the channel walls, and substitute (2.10) into (2.9), assuming $\ln(\hat{p}_{V,e}/\hat{p}_V) \approx \hat{p}_{V,e}/\hat{p}_V - 1$ and $\sqrt{\hat{T}|_{\hat{h}}} \approx \sqrt{\hat{T}_V}$. The resulting expression for the evaporative mass flux is

$$Kj = \delta(p - p_V) + T|_h, \tag{2.12}$$

where $K = \hat{k}\sqrt{2\pi \hat{R}_g^3 \hat{T}_V^5}/\hat{p}_V \hat{\mathcal{L}}^2 \hat{H} \alpha_E$ is the Knudsen number (ratio of interfacial to bulk heat transfer resistance), which is essentially the inverse of the Biot number, and

938 A22-8

$\delta = \hat{\mu}_0 \hat{U} \hat{T}_V / \hat{\rho} \epsilon \hat{H} \hat{\mathcal{L}} \Delta \hat{T}$ accounts for the effects of pressure variation on the local interface temperature (Ajaev 2005). From (2.12) it can be seen that the evaporative mass flux j is proportional to deviations from p_V and $\hat{T}_V$. Note that δ is typically $O(10^{-4} - 10^{-6})$ compared with $T|_h$ which is $O(1)$, so contributions of the $\delta(p - p_V)$ term in (2.12) are typically neglected (Markos *et al.* 2006; Murisic & Kondic 2011). However, these contributions become significant near the finger tip as $a \to 0$, where $p \to -\infty$ as seen in (2.6*d*).

2.4. *Energy transport*

Energy conservation is governed by

$$\hat{\rho} \hat{C}_p \left[\frac{\partial \hat{T}}{\partial \hat{t}} + \hat{\boldsymbol{u}} \cdot \widehat{\boldsymbol{\nabla}} \hat{T} \right] = \hat{k} \widehat{\nabla}^2 \hat{T}. \tag{2.13}$$

For simplicity, we consider the limiting case where heat conduction in the channel walls is neglected, and assume that the channel walls are held at a constant temperature $\hat{T}_W$. The energy balance at the liquid–air interface is

$$\hat{\mathcal{L}} \hat{j} = -\boldsymbol{n} \cdot \hat{k} \widehat{\boldsymbol{\nabla}} \hat{T}. \tag{2.14}$$

We render (2.13) dimensionless using the scalings in (2.3) and (2.11*a–d*). The dimensionless numbers that arise are the Reynolds number Re (see § 2.2) and the Prandtl number $Pr = \hat{\mu}_0 \hat{C}_p / \hat{k}$ (ratio of momentum to thermal diffusivity).

In the limits of $\epsilon^2 \ll 1$ and $\epsilon Re Pr \ll 1$, the leading-order energy-transport equation is

$$T_{xx} + T_{yy} = 0, \tag{2.15a}$$

subject to

$$T = 1 \quad \text{at solid boundaries} \quad \text{and} \quad j(1 + h_x^2)^{1/2} = h_x T_x - T_y \quad \text{at free surface}, \tag{2.15b}$$

where j is determined using (2.12). The total evaporative mass flux for a given channel cross-section is defined as

$$\tilde{J} = \int_S j \, \mathrm{d}S = 2 \int_{x_1}^{x_2} j(1 + h_x^2)^{1/2} \, \mathrm{d}x, \tag{2.16}$$

where x_1 and x_2 are given by (2.7). The liquid–air interface arc length is given by

$$S = \begin{cases} \dfrac{\pi - 2\theta}{\lambda \cos \theta} & \text{in meniscus-deformation regime}, \\[2mm] \dfrac{\pi - 2\theta_0}{\lambda \cos \theta_0} & \text{in meniscus-recession regime}, \\[2mm] \dfrac{(2\pi - 4\theta - 4\beta) \sin \beta}{\cos(\theta + \beta)} & \text{in corner-transition regime}, \\[2mm] \dfrac{(\pi - 4\theta) a \sin \pi/4}{\cos(\theta + \pi/4)} & \text{in corner-flow regime}, \end{cases} \tag{2.17}$$

where θ and a are dependent on (z, t) and the cross-sectional-averaged dimensionless temperature is defined as

$$\bar{T} = \frac{1}{A} \int_A T \, \mathrm{d}A, \tag{2.18}$$

where A is the liquid cross-sectional area from (2.6).

2.5. *Solute transport*

A convection–diffusion equation governs the transport of solute

$$\frac{\partial c}{\partial \hat{t}} + \hat{\boldsymbol{u}} \cdot \widehat{\boldsymbol{\nabla}} c = \hat{D} \widehat{\nabla}^2 c, \tag{2.19a}$$

where c is the solute concentration (mass fraction) and $\hat{D}$ is the diffusion coefficient, which is assumed to be constant. We impose no-flux boundary conditions

$$\hat{D}(\boldsymbol{n} \cdot \widehat{\boldsymbol{\nabla}})c = 0 \quad \text{at solid boundaries,} \tag{2.19b}$$

$$\hat{D}(\boldsymbol{n} \cdot \widehat{\boldsymbol{\nabla}})c = c(\hat{\boldsymbol{u}} - \hat{\boldsymbol{u}}_I) \cdot \boldsymbol{n} = c\hat{j}/\hat{\rho} \quad \text{at free surface,} \tag{2.19c}$$

where $\hat{\boldsymbol{u}}_I$ is the liquid–air interface velocity and $\hat{j}$ is the local evaporative mass flux. Using the scalings in (2.3), (2.19a) becomes

$$\epsilon^2 Pe(c_t + uc_x + vc_y + wc_z) = c_{xx} + c_{yy} + \epsilon^2 c_{zz}, \tag{2.20a}$$

where $Pe = \hat{U}\hat{L}/\hat{D}$ is the Péclet number (ratio of convective to diffusive transport rates). Similarly, the no-flux boundary conditions become

$$(\boldsymbol{n} \cdot \boldsymbol{\nabla})c = 0 \quad \text{at solid boundaries,} \tag{2.20b}$$

$$-h_x c_x + c_y - \epsilon^2 h_z c_z = \epsilon^2 PecEj(1 + h_x^2)^{1/2} \quad \text{at free surface,} \tag{2.20c}$$

where $E = \hat{k}\Delta\hat{T}/\hat{\rho}\hat{\mathcal{L}}\hat{H}\epsilon\hat{U}$ is the evaporation number (ratio of characteristic capillary to evaporation times).

To simplify (2.20a) further, we assume solute transport in the *x* and *y* directions is dominated by diffusion ($\epsilon^2 Pe \ll 1$). As proposed by Jensen & Grotberg (1993), we asymptotically expand the concentration in terms of $\epsilon^2 Pe$, obtaining $c(x, y, z, t) = c_0(z, t) + \epsilon^2 Pec_1(x, y, z, t)$, where we assume $\int_A c_1 \, \mathrm{d}A = 0$. This allows us to define the cross-sectional-averaged concentration as

$$\bar{c} = \frac{1}{A} \int_A c \, \mathrm{d}A = c_0(z, t). \tag{2.21}$$

We apply cross-sectional averaging to (2.20a) and replace the c_1 terms using the no-flux condition at the free surface in (2.20c). In the limit of $\epsilon^2 \ll 1$, we obtain the following evolution equation for $\bar{c}$:

$$\bar{c}_t + \bar{w}\bar{c}_z = \frac{1}{PeA}(A\bar{c}_z)_z + \frac{\bar{c}}{A}E\tilde{J}, \tag{2.22}$$

where $\bar{w}$ is the cross-sectional-averaged velocity (which will be obtained from (2.28)), A is the dimensionless cross-sectional area from (2.6), and $\tilde{J}$ is the total cross-sectional evaporative mass flux in a given channel cross-section from (2.16).

2.6. *Constitutive equations for viscosity and surface tension*

The constitutive equations for viscosity M and surface tension Σ depend on the liquid solution we choose to study. In this work, we use aqueous poly(vinyl alcohol) (PVA) solutions and compare model predictions with capillary-flow experiments conducted by Lade *et al.* (2018). An empirical model proposed by Patton (1964) is used to capture the dependence of the viscosity on $\bar{T}$ and $\bar{c}$

through

$$\log M = \frac{\bar{c}}{k_a(\bar{T}) + \bar{c}k_b(\bar{T})}, \qquad (2.23a)$$

where

$$\left.\begin{array}{l} k_a(\bar{T}) = 1.28 \times 10^{-5}(\hat{T}_V + \bar{T}\Delta\hat{T}) + 1.59 \times 10^{-2}, \\ k_b(\bar{T}) = 3.83 \times 10^{-4}(\hat{T}_V + \bar{T}\Delta\hat{T}) - 2.47 \times 10^{-2}. \end{array}\right\} \qquad (2.23b)$$

The $k_a(\bar{T})$ and $k_b(\bar{T})$ functions were reported by Lade *et al.* (2018) after fitting the empirical model to rheological data of PVA solutions for a range of temperatures and concentrations. In (2.23a), increasing the solute concentration can increase the viscosity by orders of magnitude, and increasing the temperature decreases the viscosity but does not change its order of magnitude. Similar models can be used to describe any solution or colloidal suspension where the shear viscosity is the dominant rheological parameter.

The effects of $\bar{T}$ and $\bar{c}$ on the surface tension are modelled using

$$\Sigma = 1 - Ma_c\bar{c}^{1/2} - Ma_T\bar{T}, \qquad (2.24)$$

where $Ma_c = \hat{\gamma}_c\epsilon/\hat{\mu}_0\hat{U}$ is the solutal Marangoni number and $Ma_T = \hat{\gamma}_T\Delta\hat{T}\epsilon/\hat{\mu}_0\hat{U}$ is the thermal Marangoni number, which are ratios of surface-tension-gradient forces to viscous forces, and $\hat{\gamma}_c$ and $\hat{\gamma}_T$ are experimentally obtained constants. We assume the temperature at the liquid–air interface does not deviate much from the vapour temperature, which allows us to write the surface tension as a linear function of $\bar{T}$ (Burelbach *et al.* 1988; Gramlich *et al.* 2002; Ajaev 2005; Craster, Matar & Sefiane 2009). Many prior studies assume a dilute solution and use a linearized surface-tension dependence on the concentration (e.g. Lam & Benson 1970; Pham, Cheng & Kumar 2017); this would yield results that are qualitatively similar to those obtained using (2.24). Comparison of the empirical models in (2.23a) and (2.24) with the experimental results of Lade *et al.* (2018) is found in the supplementary material available at https://doi.org/10.1017/jfm.2022. 140.

2.7. *Liquid height evolution*

We begin with the no-flux boundary condition at the free surface given by

$$(\hat{\boldsymbol{u}} - \hat{\boldsymbol{u}}_I) \cdot \boldsymbol{n} = \hat{j}/\hat{\rho}, \qquad (2.25)$$

where the velocity of the liquid–air interface is $\hat{\boldsymbol{u}}_I = (0, \hat{h}_{\hat{t}}, 0)$. Using the scalings in (2.3) and (2.11a–d), (2.25) becomes

$$-uh_x + v - wh_z - h_t = Ej(1 + h_x^2 + \epsilon^2 h_z^2)^{1/2}. \qquad (2.26)$$

We apply cross-sectional averaging to the mass conservation equation (2.4a) and replace the u and v terms using (2.26), thus obtaining

$$A_t = -(\bar{w}A)_z - E\tilde{J}, \qquad (2.27)$$

where for each regime, the dimensionless liquid cross-sectional area $A = 2\int_{x_1}^{x_2} h\,dx$ is given by (2.6), $\bar{w} = A^{-1}\int_A w\,dA$ is the cross-sectional-averaged velocity and $\tilde{J}$ is the total evaporative mass flux in a given channel cross-section from (2.16). Equation (2.27) is the mass-balance equation derived by Lenormand & Zarcone (1984), relating the time derivative of the dimensionless liquid cross-sectional area A to the gradient in the dimensionless flux $Q = \int_A w\,dA = \bar{w}A$, with an additional term accounting for mass lost due to solvent evaporation.

The velocity in (2.27) can be decomposed as follows:

$$\bar{w} = \bar{w}_{ca} + \bar{w}_{cg} + \bar{w}_{tg}, \tag{2.28}$$

where each contribution in each regime (figure 1) is expressed in (2.29). Each component corresponds to a different mechanism acting on the liquid to drive flow. Here, $\bar{w}_{ca}$ is the velocity due to capillary effects, while $\bar{w}_{cg}$ and $\bar{w}_{tg}$ correspond to the effects of Marangoni stresses. Specifically, $\bar{w}_{cg}$ is due to solute concentration gradients and $\bar{w}_{tg}$ is due to thermal gradients. For each regime these contributions are given by

$$\bar{w}_{ca} = -\frac{\bar{U}_D^c}{M} p_z, \quad \bar{w}_{cg} = \frac{\bar{U}_D^g}{M} \frac{\partial \Sigma}{\partial \bar{c}} \bar{c}_z, \quad \bar{w}_{tg} = \frac{\bar{U}_D^g}{M} \frac{\partial \Sigma}{\partial \bar{T}} \bar{T}_z, \quad \text{meniscus deformation,} \tag{2.29a}$$

$$\bar{w}_{ca} = -\frac{\bar{U}_R^c}{M} p_z, \quad \bar{w}_{cg} = \frac{\bar{U}_R^g}{M} \frac{\partial \Sigma}{\partial \bar{c}} \bar{c}_z, \quad \bar{w}_{tg} = \frac{\bar{U}_R^g}{M} \frac{\partial \Sigma}{\partial \bar{T}} \bar{T}_z, \quad \text{meniscus recession,} \tag{2.29b}$$

$$\bar{w}_{ca} = -\frac{\bar{U}_T^c}{M} p_z, \quad \bar{w}_{cg} = \frac{\bar{U}_T^g}{M} \frac{\partial \Sigma}{\partial \bar{c}} \bar{c}_z, \quad \bar{w}_{tg} = \frac{\bar{U}_T^g}{M} \frac{\partial \Sigma}{\partial \bar{T}} \bar{T}_z, \quad \text{corner transition,} \tag{2.29c}$$

$$\bar{w}_{ca} = -a^2 \frac{\bar{U}_C^c}{M} p_z, \quad \bar{w}_{cg} = \frac{\bar{U}_C^g}{M} \frac{\partial \Sigma}{\partial \bar{c}} \bar{c}_z, \quad \bar{w}_{tg} = a \frac{\bar{U}_C^g}{M} \frac{\partial \Sigma}{\partial \bar{T}} \bar{T}_z, \quad \text{corner flow,} \tag{2.29d}$$

where $\bar{U}_i^c$ and $\bar{U}_i^g$ are rescaled cross-sectional-averaged dimensionless velocities, with the subscript i being equal to D, R, T or C for the meniscus-deformation, meniscus-recession, corner-transition and corner-flow regimes, respectively. Details of the calculation of $\bar{U}_i^c$ and $\bar{U}_i^g$ can be found in the supplementary material. The expressions for M and Σ are given by (2.23a) and (2.24), respectively.

Consistent with prior studies considering horizontal rectangular channels, we neglect the meniscus-recession regime (i.e. $z_D = z_M$) where $\bar{w}_{ca} = 0$. This is because the transverse curvature gradients are zero (constant p in (2.6b)) and the only contribution to $\bar{w}_{ca}$ is from $O(\epsilon^2)$ axial curvature gradients, which we did not account for. The transition from the meniscus-deformation regime to the corner-flow regime (for $\lambda > \lambda_c$) is treated as a jump in the dimensionless liquid height $a(z, t)$ (Nilson *et al.* 2006; Kolliopoulos *et al.* 2021).

2.8. *Reservoir*

Liquid is supplied to the microchannel from a cylindrical reservoir of radius $\hat{R}$ and height $\hat{H}$, and the liquid–air interface in the reservoir is assumed to be axisymmetric. The channel inlet is assumed to have a negligible influence on the liquid–air interface in the reservoir. The reservoir aspect ratio is $\lambda_R = \hat{H}/\hat{R}$ and the cylindrical coordinates of the reservoir are scaled using $(\hat{r}, \hat{y}, \phi) = (\hat{R}r, \hat{H}y, \phi)$.

2.8.1. *Hydrodynamics*

Following a similar procedure to the one described in § 2.2, the normal stress balance in (2.1b) reduces to the Young–Laplace equation,

$$p - p_{V,T} = -\frac{\Sigma \lambda_R^2}{Ca} \left[\frac{h_{rr}}{(1 + \lambda_R^2 h_r^2)^{3/2}} + \frac{h_r}{r(1 + \lambda_R^2 h_r^2)^{1/2}} \right]. \tag{2.30}$$

Using (2.30) in combination with a condition for the contact-line location on the solid wall ($h = 1$, at $r = 1$), a symmetry condition at the reservoir centre ($h_r = 0$, at $r = 0$) and the definition of the contact angle θ_R on the solid wall ($\lambda_R h_r/[1 + \lambda_R^2 h_r^2]^{1/2} = \cos \theta_R$, at $r = 1$), we obtain the

938 A22-12

following leading-order expressions for pressure $p(t)$ and liquid–air interface profile $h(r, t)$ in the reservoir:

$$p = -2\Sigma \lambda_R \cos \theta_R(t) + p_{V,T}, \tag{2.31a}$$

$$h = 1 + \frac{\tan \theta_R(t)}{\lambda_R} - \frac{1}{\lambda_R} \left[\frac{1}{\cos^2 \theta_R(t)} - r^2 \right]^{1/2}. \tag{2.31b}$$

2.8.2. *Energy transport*

Similar to § 2.4, we consider energy conservation in the limit of $\lambda_R RePr \ll 1$, resulting in

$$\frac{\lambda_R^2}{r} (rT_r)_r + T_{yy} = 0, \tag{2.32a}$$

subject to

$$T = 1 \quad \text{at solid boundaries}, \quad \text{and} \quad j(1 + \lambda_R^2 h_r^2)^{1/2} = \lambda_R^2 h_r T_r - T_y \quad \text{at free surface.} \tag{2.32b}$$

Note that in the limit of $\lambda_R \to 0$, (2.32) solved along with (2.12) results in the evaporation models used for axisymmetric droplets and thin films, where $j = (1 + \delta(p - p_V))/(K + h)$ (Ajaev & Homsy 2001; Ajaev 2005; Pham & Kumar 2017, 2019).

The dimensionless total evaporative mass flux for a given reservoir cross-section is defined as

$$\tilde{J}_R = \int_{S_R} j \, dS_R = \int_0^1 j(1 + \lambda_R^2 h_r^2)^{1/2} r \, dr. \tag{2.33}$$

The liquid–air interface arc length of the reservoir cross-section is given by

$$S_R = \frac{1}{2} + \frac{1}{2} \left(\frac{1 - \sin \theta_R(t)}{\cos \theta_R(t)} \right)^2. \tag{2.34}$$

2.8.3. *Liquid volume evolution*

The dimensionless liquid volume in the reservoir $V_R = 2 \int hr \, dr$ is

$$V_R = 1 - \frac{1 - \sin \theta_R(t)}{6\lambda_R \cos \theta_R(t)} \left[3 + \left(\frac{1 - \sin \theta_R(t)}{\cos \theta_R(t)} \right)^2 \right], \tag{2.35}$$

where V_R is scaled by the reservoir volume $\pi \hat{R}^2 \hat{H}$. The ratio of channel to reservoir volume is $f_R = \lambda_R^2/\pi \epsilon \lambda$. The reservoir is considered depleted when the liquid–air interface contacts the reservoir bottom (i.e. $h(r = 0) = 0$ which corresponds to $\theta_R = \arcsin((1 - \lambda_R^2)/(1 + \lambda_R^2))$ and $V_R = (3 - \pi \epsilon \lambda f_R)/6)$.

We model the evolution of V_R through the following total mass balance:

$$(V_R)_t = -f_R \lambda \bar{w} A|_{z=0} - 2E\tilde{J}_R, \tag{2.36}$$

where the rate of change of liquid volume in the reservoir is equal to the liquid flux into the channel plus the liquid lost to evaporation. Evaporation is accounted for through the total evaporative mass flux for a given reservoir cross-section $\tilde{J}_R$ using (2.33).

2.8.4. *Solute transport*

The solute concentration in the reservoir c_R is assumed to be spatially uniform and its evolution is modelled using the following species mass balance:

$$(c_R V_R)_t = -f_R \lambda \bar{w} \bar{c} A|_{z=0}, \tag{2.37}$$

where the rate of change of solute mass in the reservoir is equal to the solute mass flux into the channel.

3. Numerical methods

3.1. *Boundary conditions*

At the channel inlet ($z = 0$; see figure 1), the pressure and solute concentration are matched to the reservoir pressure and solute concentration, respectively, and the liquid height is assumed to be pinned to the top of the channel sidewall. This results in the following conditions at the channel inlet:

$$\theta(0, t) = \cos^{-1}\left[\lambda_R \cos\theta_R(t)/\lambda\right], \quad a(0, t) = 1, \quad \text{and} \quad \bar{c}(0, t) = c_R(t). \tag{3.1a–c}$$

Note that the condition on the contact angle at the channel inlet is obtained by matching the pressure in (2.6a) and (2.31a).

For $\lambda \geq \lambda_c$, at the transition from the meniscus-deformation to corner-flow regime ($z = z_M$), we impose the following boundary conditions:

$$\left.\begin{aligned}
\theta(z_M^-, t) = \theta(z_M^+, t) = \theta_0, \quad a(z_M^-, t) = 1, \quad a(z_M^+, t) = \lambda_c/\lambda, \\
\bar{c}(z_M^-, t) = \bar{c}(z_M^+, t), \quad \text{and} \quad A\bar{c}_z|_{z=z_M^-} = A\bar{c}_z|_{z=z_M^+},
\end{aligned}\right\} \tag{3.2}$$

where the boundary conditions on θ and a are discussed in § 2.1 and the boundary conditions on $\bar{c}$ physically represent mass continuity with no accumulation at the interface between the two regimes.

For $\lambda < \lambda_c$, at the transition from the meniscus-deformation to corner-transition regime ($z = z_M$), we impose the following boundary conditions

$$\left.\begin{aligned}
\theta(z_M^-, t) = \theta_C, \quad \theta(z_M^+, t) = \theta_T, \quad a(z_M^-, t) = a(z_M^+, t) = 1, \\
\bar{c}(z_M^-, t) = \bar{c}(z_M^+, t), \quad \text{and} \quad A\bar{c}_z|_{z=z_M^-} = A\bar{c}_z|_{z=z_M^+}.
\end{aligned}\right\} \tag{3.3}$$

Here, $\theta_C = \arcsin[(1 - 4\lambda^2)/(1 + 4\lambda^2)]$ is the critical angle at which the upper meniscus touches the channel bottom and θ_T (§ 2.1) is the angle determined (via Newton's method) by setting $A(z_M^-, t) = A(z_M^+, t)$ to conserve mass. At the transition from the corner-transition to corner-flow regime ($z = z_C$), we impose the following boundary conditions:

$$\left.\begin{aligned}
\theta(z_C^-, t) = \theta(z_C^+, t) = \theta_0, \quad a(z_C^-, t) = a(z_C^+, t) = 1, \\
\bar{c}(z_C^-, t) = \bar{c}(z_C^+, t), \quad \text{and} \quad A\bar{c}_z|_{z=z_C^-} = A\bar{c}_z|_{z=z_C^+}.
\end{aligned}\right\} \tag{3.4}$$

Finally, at the end of the corner-flow regime ($z = z_T$) we impose

$$\theta(z_T, t) = \theta_0, \quad a(z_T, t) = 0, \quad \text{and} \quad \bar{c}_z(z_T, t) = 0. \tag{3.5a–c}$$

The boundary condition on $\bar{c}$ in (3.5a–c) corresponds to no flux. The boundary conditions in (3.2)–(3.5a–c) for the contact angle θ and the liquid height a on the channel sidewall were also used by Kolliopoulos *et al.* (2021).

3.2. *Initial conditions*

Initial conditions for $\theta(z, t_0)$, $a(z, t_0)$, $z_M(t_0)$, $z_C(t_0)$ and $z_T(t_0)$ are generated using the similarity solutions reported by Kolliopoulos *et al.* (2021) in the absence of evaporation ($E = 0$). The reported solutions are in terms of the self-similar variable $\eta = z/\sqrt{t}$, so we determine the initial interface profile and its axial coordinates $z = \eta\sqrt{t_0}$ by setting $t_0 = 10^{-4}$. The chosen t_0 does not influence our results since total flow times are $O(10 - 10^2)$. Additionally, we assume the reservoir is initially fully filled and the solute concentration is uniform in the reservoir and channel. Hence,

$$V_R(t_0) = 1, \quad c_R(t_0) = C_0, \quad \text{and} \quad \bar{c}(z, t_0) = C_0. \tag{3.6a–c}$$

3.3. *Solution procedure*

The rescaled cross-sectional-averaged dimensionless velocities $\bar{U}_i^c$ and $\bar{U}_i^g$ in (2.29) are calculated as discussed in the supplementary material. Velocity fields are numerically solved for with a Galerkin finite-element method using quadratic basis functions (Kolliopoulos *et al.* 2021). Results for $\bar{U}_D^c$ and $\bar{U}_T^c$ are found to be in agreement with results of Tchikanda *et al.* (2004) and Weislogel & Nardin (2005), respectively. Results for $\bar{U}_C^c$ agree with results of Ayyaswamy, Catton & Edwards (1974), Ransohoff & Radke (1988) and Yang & Homsy (2006). Additionally, results for $\bar{U}_D^g$ and $\bar{U}_C^g$ are in agreement with results of Tchikanda *et al.* (2004) and Yang & Homsy (2006), respectively.

Rather than consider effects of $a(z, t)$ and $\theta(z, t)$ on $\bar{U}_i^c$ and $\bar{U}_i^g$ separately, we consider the dependence of $\bar{U}_i^c$ and $\bar{U}_i^g$ on the liquid saturation λA (ratio of channel cross-sectional area filled with liquid to total channel cross-sectional area). These rescaled cross-sectional-averaged dimensionless velocities $\bar{U}_i^c(\lambda A)$ and $\bar{U}_i^g(\lambda A)$ are fitted with Chebyshev polynomials of the first kind using the least-squares method and then applied to calculate the cross-sectional-averaged dimensionless velocity components of $\bar{w}$ in (2.29).

The dimensionless total evaporative mass fluxes and cross-sectional-averaged dimensionless temperatures for the channel and reservoir are calculated as discussed in § 2.4 and § 2.8.2, respectively. Temperature fields are numerically solved for with a Galerkin finite-element method using quadratic basis functions. Results for $\tilde{J}$ in the corner-flow regime agree with results of Markos *et al.* (2006). Results for $\tilde{J}(\lambda A)$ and $\bar{T}(\lambda A)$ in each regime, and $\tilde{J}_R(V_R)$ and $\bar{T}(V_R)$ for the reservoir, are fitted with Chebyshev polynomials of the first kind using the least-squares method and then applied in (2.27), (2.22), (2.36) and (2.37).

For $\lambda \geq \lambda_c$, the system of equations consists of (2.27) and (2.22) for each regime in the channel (meniscus-deformation and corner-flow regimes), and (2.36) and (2.37) for the reservoir. Additionally, the positions of the moving regime boundaries are determined using the global continuity equation assuming no accumulation at the interface between two regimes, as discussed by Kolliopoulos *et al.* (2021). The general form of the global continuity equation at the interface at position z_i is

$$\left[\int_A \boldsymbol{n} \cdot (\boldsymbol{u} - \boldsymbol{u}_I) \, dA \right]_{z=z_i^-} = \left[\int_A \boldsymbol{n} \cdot (\boldsymbol{u} - \boldsymbol{u}_I) \, dA \right]_{z=z_i^+} \quad \text{at } z = z_i, \tag{3.7}$$

where $\boldsymbol{n} = (0, 0, 1)$ is the unit normal to the interface, $\boldsymbol{u} = (u, v, w)$ is the dimensionless liquid velocity, $\boldsymbol{u}_I = (0, 0, dz_i/dt)$ is the interface velocity at position z_i and A is the liquid cross-sectional area at position z_i. For the meniscus position z_M and finger tip position z_T, (3.7) reduces to

$$\left[A\bar{w} - A\frac{dz_M}{dt} \right]_{z=z_M^-} = \left[A\bar{w} - A\frac{dz_M}{dt} \right]_{z=z_M^+} \quad \text{at } z = z_M, \tag{3.8a}$$

and

$$\bar{w}|_{z=z_T^-} = \frac{dz_T}{dt} \quad \text{at } z = z_T. \tag{3.8b}$$

For $\lambda < \lambda_c$, the system of equations consists of (2.27) and (2.22) for each regime in the channel (meniscus-deformation, corner-transition and corner-flow regimes), along with (2.36) and (2.37) for the reservoir. In addition to the global continuity equations in (3.8) to determine z_M and z_T, we use

$$\left[A\bar{w} - A\frac{dz_C}{dt} \right]_{z=z_C^-} = \left[A\bar{w} - A\frac{dz_C}{dt} \right]_{z=z_C^+} \quad \text{at } z = z_C, \tag{3.9}$$

to determine z_C.

$\hat{\rho}$ (kg m^{-3})	10^3	$\hat{D}$ (m^2 s^{-1})	8.87×10^{-10}
$\hat{\gamma}_T$ (N m^{-1} K^{-1})	1.14×10^{-4}	C_0 (wt%)	3
$\hat{\sigma}_0$ (N m^{-1})	7.14×10^{-2}	$\hat{\gamma}_c$ (N m^{-1})	3.86×10^{-2}
$\hat{\mu}_0$ (Pa s)	9.35×10^{-4}	$\hat{H}$ (μm)	25–50
$\hat{k}$ (W m^{-1} K^{-1})	0.605	$\hat{W}$ (μm)	10–200
$\hat{C}_p$ (J kg^{-1} K^{-1})	4180	$\hat{L}$ (mm)	30
$\hat{\mathcal{L}}$ (J kg^{-1})	2.442×10^6	$\hat{R}$ (mm)	0.4–100
$\hat{R}_g$ (J kg^{-1} K^{-1})	461.5	$\Delta\hat{T}$ (K)	0–40
θ_0 (deg.)	19.9 (water), 24.5 (PVA)	R_H	0–1

Table 1. Typical dimensional parameter values at 298 K and 1 atm (Lade *et al.* 2018; Kolliopoulos *et al.* 2019). Contact angles are for a substrate made of NOA73 (UV-curable adhesive used by Lade *et al.* (2018) to fabricate microchannels).

The spatial derivatives in both systems of equations are approximated with second-order centred finite differences. The resulting discretized systems of ordinary differential equations are solved using the fully implicit, variable-step and variable-order **ode15i** solver in MATLAB.

Numerical solutions for the dimensionless total evaporative mass flux $\tilde{J}(\lambda A)$ and cross-sectional-averaged dimensionless temperature $\bar{T}(\lambda A)$ for the channel and their dependence on the channel aspect ratio λ and equilibrium contact angle θ_0 are presented first (§ 4.1). Using these numerical solutions we then consider capillary flow of an evaporating pure solvent (§ 4.2) and liquid solution (§ 5) for $\lambda \geq \lambda_c$ and $\lambda < \lambda_c$. Finally, model predictions for aqueous PVA solutions are compared with experimental results of Lade *et al.* (2018) (§ 6).

4. Results: pure solvents

4.1. *Evaporative mass flux*

As discussed in § 2.1, the free-surface morphology is determined by the liquid height $a(z, t)$ and the contact angle $\theta(z, t)$ on the channel sidewall (figure 1). However, rather than consider effects of $a(z, t)$ and $\theta(z, t)$ on the dimensionless total evaporative mass flux $\tilde{J}$ and the cross-sectional-averaged dimensionless temperature $\bar{T}$ separately, we consider the dependence of $\tilde{J}$ and $\bar{T}$ on the liquid saturation λA (ratio of channel cross-sectional area filled with liquid to total channel cross-sectional area). Since for a given microchannel λ is constant, we vary A to obtain $\tilde{J}(\lambda A)$ and $\bar{T}(\lambda A)$ for the channel cross-sections seen in figure 1. Note that $\lambda A = 1$ corresponds to a fully filled channel cross-section ($\theta = \pi/2$) and $\lambda A = 0$ corresponds to an empty channel cross-section ($a = 0$).

Numerical solutions for $\tilde{J}(\lambda A)$ and $\bar{T}(\lambda A)$ are obtained using (2.16) and (2.18), respectively, after solving (2.15) as discussed in § 3.3. Motivated by the experiments of Lade *et al.* (2018), we consider water as the solvent. Typical dimensional parameter values are shown in table 1 and order-of-magnitude estimates of key dimensionless parameters are given in table 2. In this section we choose representative parameter values $R_H = 1$, $\Delta\hat{T} = 40$ K, $\hat{H} = 50\,\mu$m and $\alpha_E = 5 \times 10^{-3}$, since changes in these parameters do no qualitatively change the results. The dimensionless parameters K and δ are calculated based on values in table 1.

In figures 2(*a*) and 2(*b*), we consider $\tilde{J}(\lambda A)$ for different channel aspect ratios λ and equilibrium contact angles θ_0, respectively. Solid lines represent the numerical results and symbols represent the bounds of each regime in figure 1. For $\lambda \geq \lambda_c$, decreasing λA leads to the transition from the meniscus-deformation regime to the corner-flow regime (circles), where a jump in λA (dotted lines) is observed due to neglecting the meniscus-recession regime as discussed in § 2.7. In the

Parameter	Physical Meaning	Order of magnitude
$\epsilon = \hat{H}/\hat{L}$	channel height/channel length	10^{-3}
$\lambda = \hat{H}/\hat{W}$	channel height/channel width	0.1–1
$\lambda_R = \hat{H}/\hat{R}$	channel height/reservoir radius	0.1–1
$f_R = \lambda_R^2/\pi\epsilon\lambda$	channel volume/reservoir volume	0–10
$Re = \hat{\rho}\hat{U}\hat{H}/\hat{\mu}_0$	inertial forces/viscous forces	10
$Ca = \hat{\mu}_0\hat{U}/\epsilon\hat{\sigma}_0$	viscous forces/surface-tension forces	1
$Bo = \hat{\rho}\hat{g}\hat{H}^2/\hat{\sigma}_0$	gravitational forces/surface-tension forces	10^{-4}
$K = \hat{k}\sqrt{2\pi\hat{R}_g^3\hat{T}_V^5/\hat{p}_V\hat{\mathcal{L}}^2\hat{H}\alpha_E}$	interfacial heat transfer resistance/bulk heat transfer resistance	1–10
$\delta = \hat{\mu}_0\hat{U}\hat{T}_V/\hat{\rho}\epsilon\hat{H}\hat{\mathcal{L}}\Delta\hat{T}$	pressure effects on local interface temperature	10^{-4}–10^{-6}
$Pr = \hat{\mu}_0\hat{C}_p/\hat{k}$	momentum diffusivity/thermal diffusivity	10
$Pe = \hat{U}\hat{L}/\hat{D}$	convective transport rate/diffusive transport rate	10^5–10^6
$E = \hat{k}\Delta\hat{T}/\hat{\rho}\hat{\mathcal{L}}\hat{H}\epsilon\hat{U}$	capillary time/evaporation time	0–1
$Ma_T = \hat{\gamma}_T\Delta\hat{T}\epsilon/\hat{\mu}_0\hat{U}$	surface-tension-gradient forces/viscous forces	0–1
$Ma_c = \hat{\gamma}_c\epsilon/\hat{\mu}_0\hat{U}$	surface-tension-gradient forces/viscous forces	0–1

Table 2. Order-of-magnitude estimates of key dimensionless parameters calculated using parameter values in table 1.

corner-flow regime, λA continues to decrease until $\lambda A = 0$, corresponding to the finger tip. For $\lambda < \lambda_c$, decreasing λA results in the transition from the meniscus-deformation regime to the corner-transition regime (circles) and further decreasing λA results in the transition from the corner-transition regime to the corner-flow regime (squares).

In both figures 2(a) and 2(b), $\tilde{J}$ is a non-monotonic function of λA. In the meniscus-deformation regime, decreasing λA increases $\tilde{J}$ because the liquid–air interface approaches the channel bottom and the liquid–air interface arc length S (see (2.17)) increases. For $\lambda < \lambda_c$, a jump in $\tilde{J}$ is observed at the transition from the meniscus-deformation regime to the corner-transition regime (circles) due to the difference in S caused by the difference in contact angles on the channel sidewall and bottom on either side of the transition (see § 2.1). Finally, in the corner-transition regime and corner-flow regime, decreasing λA decreases $\tilde{J}$ due to the decrease in S.

In figures 2(c) and 2(d), we consider $\bar{T}(\lambda A)$ for different channel aspect ratios λ and equilibrium contact angles θ_0, respectively. Unlike $\tilde{J}$, there is a monotonic increase in $\bar{T}$ with decreasing λA, due to the liquid–air interface moving closer to the channel bottom.

In prior studies, the pressure contributions to the local interface temperature are neglected (Markos *et al.* 2006) by neglecting $\delta(p - p_V)$ in (2.12). This assumption, along with rescaling the liquid–air interface arc length as $S' = S/a$, where a is the liquid height on the channel sidewall, allows for $\tilde{J}$ in the corner-flow regime to be expressed as

$$\tilde{J} = \frac{a}{a_C}\tilde{J}(\lambda A_C), \tag{4.1a}$$

where

$$A_C = \frac{B(\theta_0, \theta_0)a_C^2}{(\cos\theta_0 - \sin\theta_0)^2}, \tag{4.1b}$$

$$a_C = \begin{cases} \lambda/\lambda_c, & \text{if } \lambda \geq \lambda_c, \\ 1, & \text{if } \lambda < \lambda_c, \end{cases} \tag{4.1c}$$
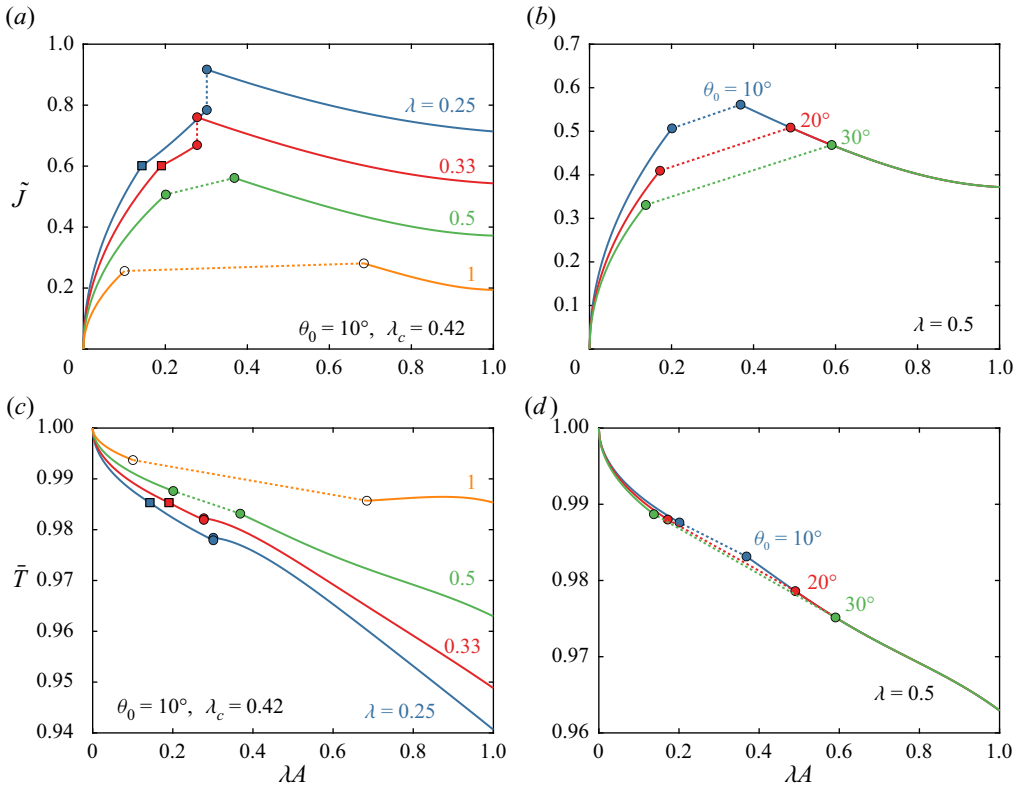
Figure 2. Dimensionless total evaporative mass flux $\tilde{J}$ as a function of liquid saturation λA for different (a) channel aspect ratios λ and (b) equilibrium contact angles θ_0. Cross-sectional-averaged dimensionless temperature $\bar{T}$ as a function of liquid saturation λA for different (c) channel aspect ratios λ and (d) equilibrium contact angles θ_0. Solid lines represent numerical results, dotted lines represent jumps in various quantities and symbols represent the bounds of each regime. Results are for $R_H = 1$, $K = 4.88$, $\delta = 4.36 \times 10^{-6}$ and $\alpha_E = 5 \times 10^{-3}$.

where $\tilde{J}(\lambda A_C)$ is the dimensionless total evaporative mass flux at the beginning of the corner-flow regime. Neglecting $\delta(p - p_V)$ in (2.12) also allows for $\bar{T}$ in the corner-flow regime to be written as

$$\bar{T} = \frac{a}{a_C}\left[\bar{T}(\lambda A_C) - 1\right] + 1, \tag{4.2}$$

where $\bar{T}(\lambda A_C)$ is the cross-sectional-averaged dimensionless temperature at the beginning of the corner-flow regime.

In figure 3, we examine the effect of neglecting the pressure contributions to the local interface temperature in the corner-flow regime and their influence on $\tilde{J}$ and $\bar{T}$. We compare numerical results (circles), which include the $\delta(p - p_V)$ terms, with the expressions for $\tilde{J}$ and $\bar{T}$ (lines) in (4.1a) and (4.2), respectively. In both figures 3(a) and 3(b), (4.1a) and (4.2) agree with the numerical results for larger a but overpredict the numerical results for smaller a. Pressure contributions to the local interface temperature are expected to become important as the $\delta(p - p_V)$ term in (2.12) becomes $O(1)$. Since the results in figure 3 are for $\delta = 4.36 \times 10^{-6}$, using (2.6d) suggests that the $\delta(p - p_V)$ term becomes important when $a < \delta$, which is consistent with our observations (see dashed lines in figure 3). Therefore, the effects of pressure on the local interface temperature must be accounted for near the finger tip as $a \to 0$.
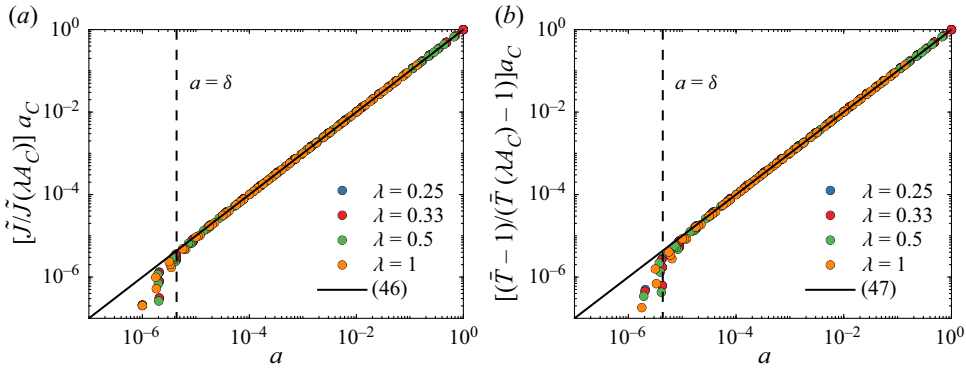
938 A22-18

Figure 3. Normalized (*a*) total evaporative mass flux $\tilde{J}$ and (*b*) cross-sectional-averaged dimensionless temperature $\bar{T}$ in the corner-flow regime as a function of the liquid height on the channel sidewalls *a*. Filled symbols represent numerical results, solid lines represent predictions of (*a*) (4.1*a*) and (*b*) (4.2), and dashed lines represent $a = \delta$. Each λ includes results for $\theta_0 = 10°, 20°$ and $30°$. The parameter values are $R_H = 1$, $K = 4.88$, $\delta = 4.36 \times 10^{-6}$ and $\alpha_E = 5 \times 10^{-3}$.
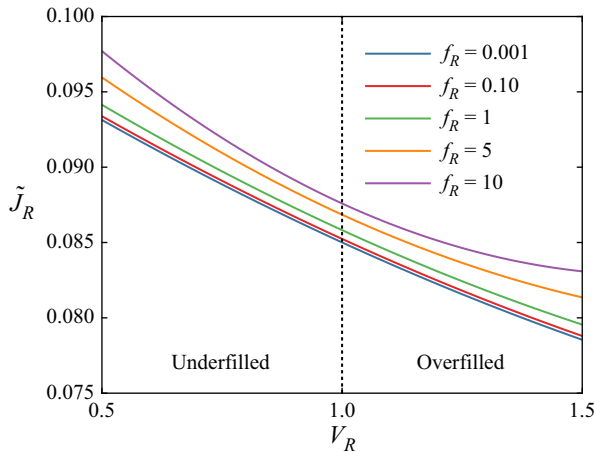
Figure 4. Dimensionless total evaporative mass flux in the reservoir $\tilde{J}_R$ as a function of the reservoir liquid volume V_R for different channel-to-reservoir volume ratios f_R. The parameter values are $R_H = 1$, $K = 4.88$, $\delta = 4.36 \times 10^{-6}$ and $\alpha_E = 5 \times 10^{-3}$.

Numerical solutions for the dimensionless total evaporative mass flux in the reservoir $\tilde{J}_R$ are obtained using (2.33), after solving (2.32) as discussed in § 3.3. In figure 4 the total dimensionless evaporative mass flux in the reservoir $\tilde{J}_R$ as a function of the liquid volume in the reservoir V_R is shown for different reservoir sizes. Here, $V_R < 1$ and $V_R > 1$ correspond to an underfilled and overfilled reservoir, respectively. Note that the contact line is assumed to be pinned to the top of the reservoir sidewall. Decreasing V_R (decreasing θ_R in (2.35)) results in a monotonic increase in $\tilde{J}_R$ because the liquid–air interface approaches the reservoir bottom and the liquid–air interface arc length S_R (see (2.34)) increases. The effect of the reservoir size is probed using the channel-to-reservoir volume ratio $f_R = \lambda_R^2 / \pi \epsilon \lambda$, where an increase in f_R (λ_R increases) leads to an increase in $\tilde{J}_R$ since the contribution to evaporation from the reservoir sidewalls increases.
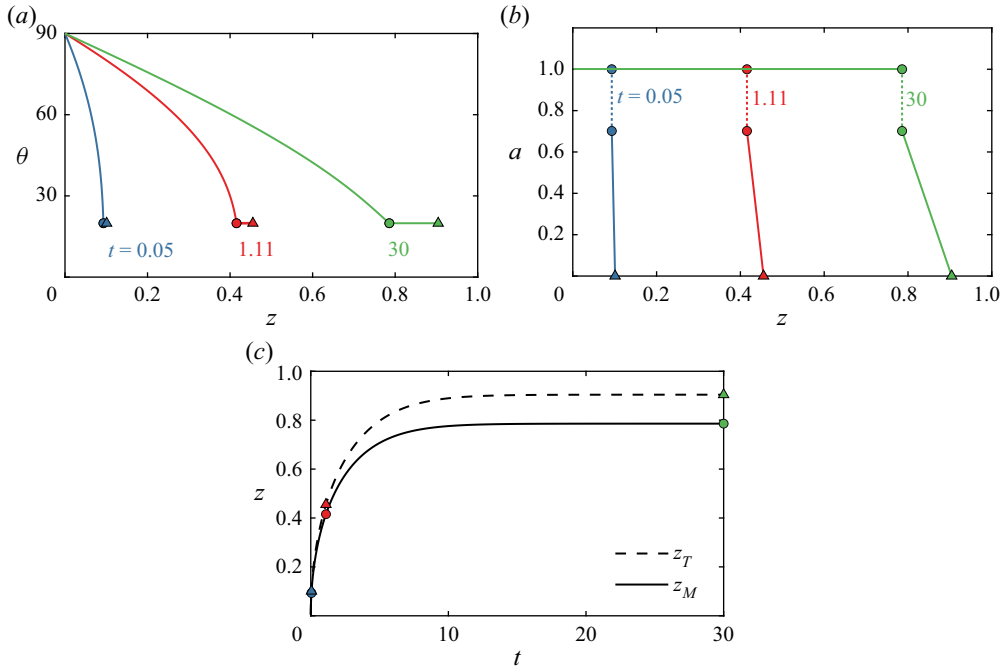
938 A22-19

Figure 5. Evolution of (*a*) contact angle on channel sidewall θ, (*b*) liquid height on channel sidewall a and (*c*) finger tip position z_T and meniscus position z_M. The parameter values are $\theta_0 = 19.9°$, $\lambda = 0.5$ ($\lambda_c = 0.35$), $\epsilon = 1.7 \times 10^{-3}$, $f_R = 0$, $C_0 = 0$, $R_H = 1$, $E = 0.93$, $Ma_T = 6.39 \times 10^{-2}$, $K = 4.88$, $\delta = 4.36 \times 10^{-6}$ and $\alpha_E = 5 \times 10^{-3}$.

4.2. *Capillary flow*

We now use results of § 4.1 to study pure water in an open rectangular channel, which allows us to isolate the influence of thermal effects on the flow. Two key dimensionless parameters that arise are the thermal Marangoni number Ma_T and the evaporation number E (table 2). Thermal Marangoni effects are retained ($Ma_T = 6.39 \times 10^{-2}$) for completeness, although qualitatively similar results are obtained in the absence of thermal Marangoni effects ($Ma_T = 0$) (see figure 8*c*). The slenderness parameter ϵ is fixed to a representative value based on the quantities given in table 1. We present numerical solutions of the contact angle $\theta(z, t)$ and the liquid height $a(z, t)$ on the channel sidewall for $\lambda > \lambda_c$ and $\lambda < \lambda_c$ in figures 5 and 6, respectively. Solutions for $\lambda > \lambda_c$ and $\lambda < \lambda_c$ are obtained by solving (2.27) for each regime in figure 1. These solutions are valid for intermediate times, when channel entrance and end effects can be neglected.

We initially consider results for $\lambda > \lambda_c$ in figures 5(*a*) and 5(*b*). Here, we assume an infinite reservoir ($f_R = 0$), so we do not include (2.36) in our governing equations. The inlet conditions are $\theta(0, t) = 90°$ and $a(0, t) = 1$ corresponding to a fully filled channel cross-section. Moving down the length of the channel, $\theta(z, t)$ decreases monotonically while $a(z, t) = 1$, and at the meniscus position z_M (circles) the flow transitions from the meniscus-deformation regime to the corner-flow regime (figure 1*a*). A jump in $a(z_M, t)$ (dashed lines) is observed at the transition in figure 5(*b*) because the meniscus-recession regime is neglected as discussed in § 2.7. In the corner-flow regime, $\theta(z, t) = \theta_0$ and $a(z, t)$ decreases monotonically until $a(z_T, t) = 0$ at the finger tip position z_T (triangles).

The evolution of the meniscus position z_M and finger tip position z_T is shown in figure 5(*c*), where both asymptotically approach their maximum values corresponding to the steady-state solution of (2.27). At this steady-state capillary flow is balanced by evaporation due to the infinite
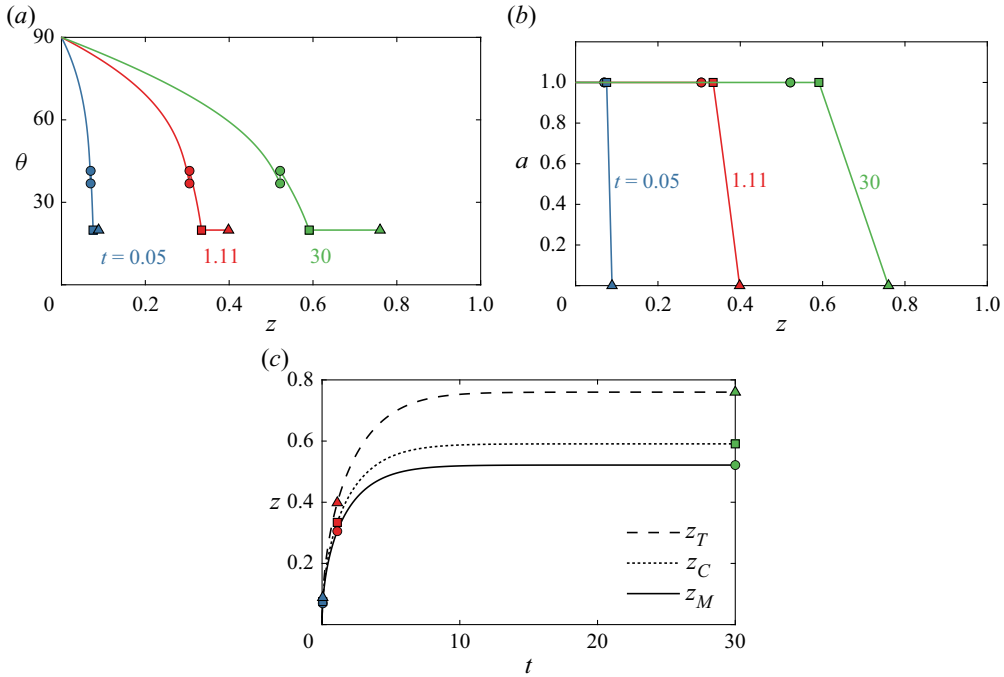
Figure 6. Evolution of (*a*) contact angle on channel sidewall θ, (*b*) liquid height on channel sidewall a and (*c*) finger tip position z_T, finger depinning position z_C and meniscus position z_M. The parameter values are $\theta_0 = 19.9°$, $\lambda = 0.25$ ($\lambda_c = 0.35$), $\epsilon = 1.7 \times 10^{-3}$, $f_R = 0$, $C_0 = 0$, $R_H = 1$, $E = 0.93$, $Ma_T = 6.39 \times 10^{-2}$, $K = 4.88$, $\delta = 4.36 \times 10^{-6}$ and $\alpha_E = 5 \times 10^{-3}$.

supply of liquid at the channel inlet from the reservoir. The evolution of z_M and z_T is qualitatively different from that observed in the absence of evaporation, where z_M and z_T scale as $\sim t^{1/2}$ (Kolliopoulos *et al.* 2021). This deviation from the Lucas–Washburn scaling for the finger tip position z_T was also observed by Gambaryan-Roisman (2019) in calculations involving V-shaped channels.

We now consider the case $\lambda < \lambda_c$ in figures 6(*a*) and 6(*b*). Moving down the length of the channel, $\theta(z, t)$ decreases monotonically while $a(z, t) = 1$. At the meniscus position z_M, the flow transitions from the meniscus-deformation regime to the corner-transition regime (figure 1*b*). A jump in $\theta(z_M, t)$ (circles) is observed at the transition in figure 6(*a*) because when the upper meniscus touches the channel bottom it is assumed that the contact angle at the channel bottom instantaneously reaches θ_0. Thus, to conserve mass, the contact angle on the channel sidewall increases as discussed in § 2.1.

In the corner-transition regime (segment from circle to square), $\theta(z, t)$ continues to monotonically decrease while $a(z, t) = 1$. At the finger depinning position z_C (squares), the flow transitions from the corner-transition regime to the corner-flow regime (figure 1*b*). In the corner-flow regime, $\theta(z, t) = \theta_0$ and $a(z, t)$ decreases monotonically until $a(z_T, t) = 0$ at the finger tip position z_T (triangles). It is evident from figure 6(*c*) that z_M, z_C and z_T deviate from the Lucas–Washburn scaling for $\lambda < \lambda_c$ as well and asymptotically approach their maximum values corresponding to the steady-state solution of (2.27).

Results for $\theta(z, t)$ and $a(z, t)$ from figures 5 and 6 are used in (2.6) to determine the evolution of the three-dimensional liquid height profile $h(x, z, t)$ in the channel, whose top view is depicted in figures 7(*a*) ($\lambda > \lambda_c$) and 7(*b*) ($\lambda < \lambda_c$), with $t = 30$ being in the steady-state regime.
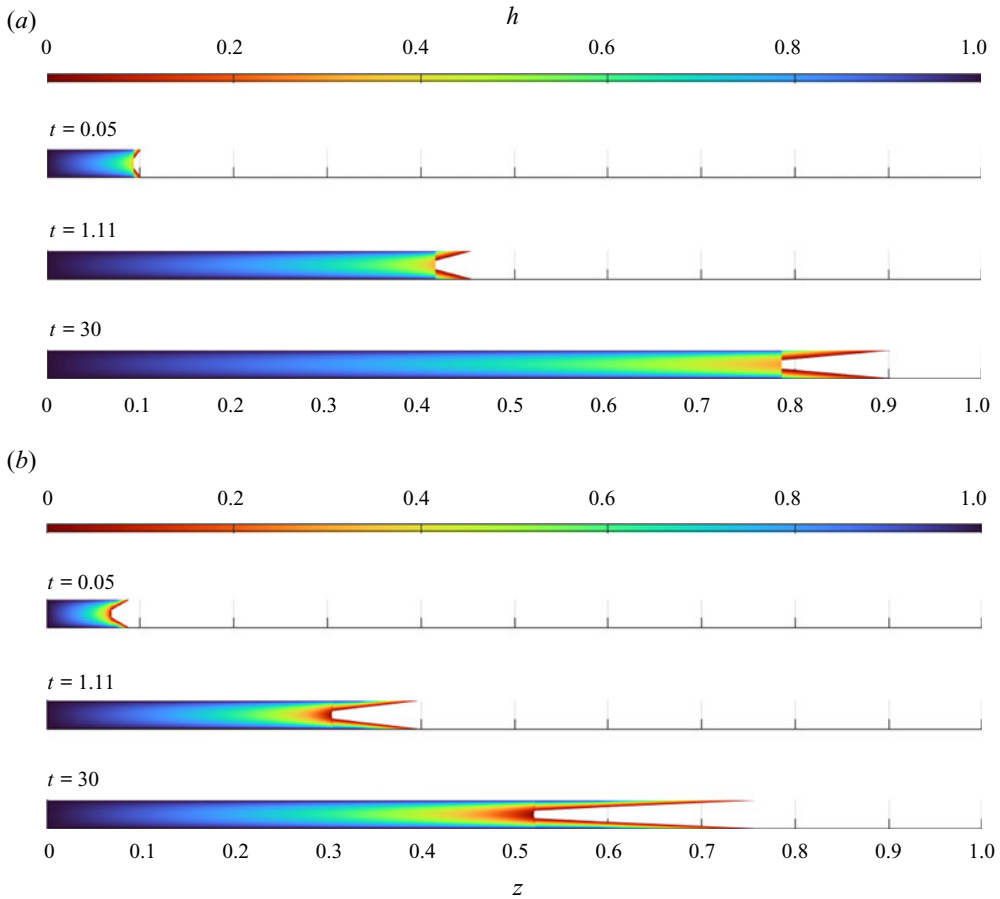
938 A22-21

Figure 7. Evolution of liquid height profile h (top view) for (a) $\lambda = 0.5$ and (b) $\lambda = 0.25$. The corresponding parameter values are given in the captions of figures 5 and 6, respectively. Discontinuities in h are caused by discontinuities in θ and a seen in figures 5 and 6.

For larger λ (figure 7a) we observe shorter fingers and longer flow distances compared with smaller λ (figure 7b). While here we considered water with $\theta_0 = 19.9°$ ($\lambda_c = 0.35$), qualitatively similar profiles are seen for liquids with $\theta_0 < \pi/4$. For liquids with $\theta_0 \geq \pi/4$ finger formation is not observed (Concus & Finn 1969).

We now examine the effect of channel aspect ratio λ, evaporation number E, thermal Marangoni number Ma_T and channel-to-reservoir volume ratio f_R on the maximum values of z_T, z_C and z_M. From figure 8(a) it is seen that when $\lambda \gg \lambda_c$ ($\lambda_c = 0.35$) the size of the meniscus-deformation regime size dominates that of the corner-flow regime (i.e. $z_M > z_T - z_M$ in figure 1a). With decreasing λ, the finger length $z_T - z_M$ increases monotonically. However, with decreasing λ the meniscus position z_M increases and then decreases. When λ drops below $\lambda_c = 0.35$, the corner-transition regime appears, and as λ is further decreased $z_T - z_M$ continues to increase. These trends are observed for other θ_0 and are consistent with trends observed by Kolliopoulos *et al.* (2021) in the absence of evaporation. Therefore, there are optimal channel aspect ratios λ for maximizing the total flow distance of the finger tip and meniscus.

In the absence of evaporation ($E = 0$) the liquid reaches the end of the channel ($z = 1$). Figure 8(b) shows that increasing the evaporation number E (increasing the substrate temperature T_W or lowering the relative humidity R_H) monotonically decreases the maximum values of z_T, z_C
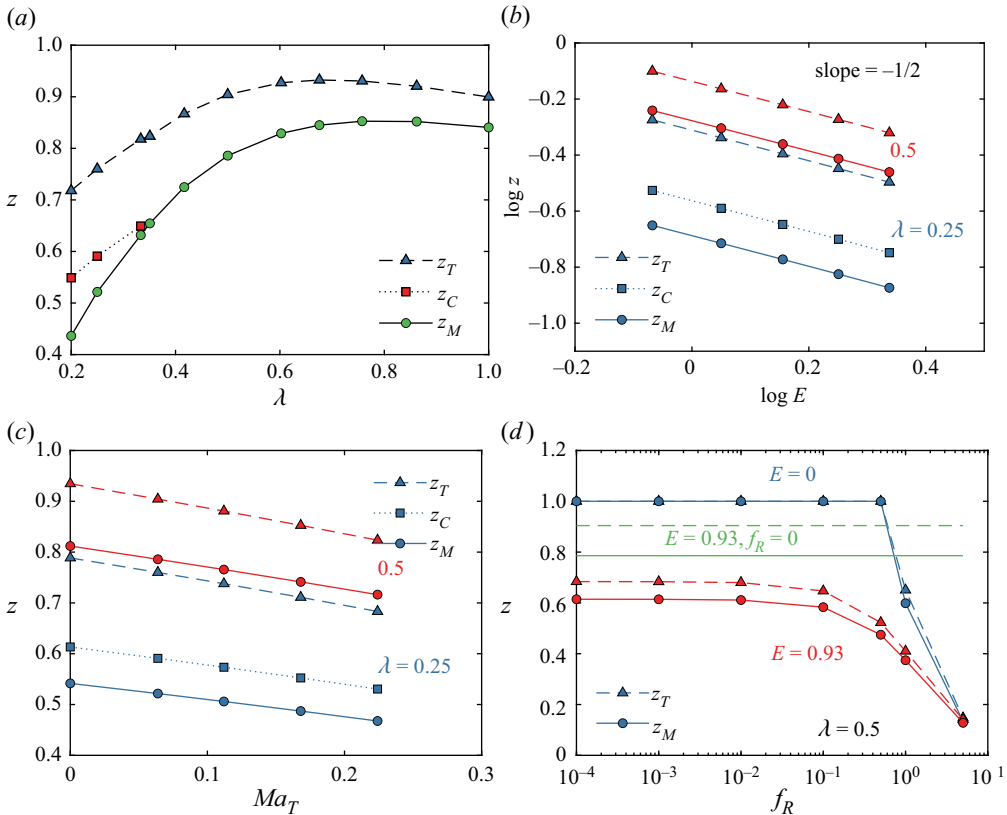
938 A22-22

Figure 8. Final finger tip position z_T, finger depinning position z_C and meniscus position z_M as a function of (a) channel aspect ratio λ, (b) evaporation number E, (c) thermal Marangoni number Ma_T and (d) channel-to-reservoir volume ratio f_R. Unless denoted otherwise, the parameter values are $\theta_0 = 19.9°$ ($\lambda_c = 0.35$), $\epsilon = 1.7 \times 10^{-3}$, $f_R = 0$, $C_0 = 0$, $R_H = 1$, $E = 0.93$, $Ma_T = 6.39 \times 10^{-2}$, $K = 4.88$, $\delta = 4.36 \times 10^{-6}$ and $\alpha_E = 5 \times 10^{-3}$.

and z_M. These maximum values are found to scale as $\sim E^{-1/2}$, which is consistent with studies of uniform evaporation in open rectangular channels (Nilson *et al.* 2006; Kolliopoulos *et al.* 2019), and uniform and diffusion-limited evaporation in V-shaped channels (Gambaryan-Roisman 2019).

The thermal Marangoni number Ma_T controls the magnitude of the surface-tension-gradient forces caused by thermal gradients. In figure 8(c) it is shown that the maximum values of z_T, z_C and z_M for all λ decrease with increasing Ma_T. This is because the cross-sectional-averaged temperature $\bar{T}$ increases down the length of the channel (figures 2c and 2d) causing the surface tension Σ to decrease due to (2.24). Decreasing Σ decreases the magnitude of the capillary-pressure gradients in $\bar{w}_{ca}$ (which drive flow) and increases the magnitude of the thermal Marangoni stresses in $\bar{w}_{tg}$ (which inhibit flow), thus reducing the axial velocity and propagation of the liquid front. Hence, increasing Ma_T decreases the axial velocity and leads to shorter flow distances.

The channel-to-reservoir volume ratio f_R provides a measure of the relative size of the channel compared with the reservoir. We examine the case where the reservoir is initially fully filled ($V_R = 1$) and consider the reservoir to be depleted when the liquid–air interface contacts the reservoir bottom ($V_R = (3 - \pi\epsilon\lambda f_R)/6$). In figure 8(d), we consider the finite-size reservoir
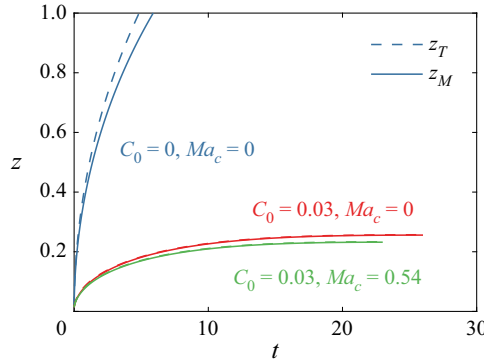
Figure 9. Evolution of finger tip position z_T and meniscus position z_M for a pure solvent ($C_0 = 0$, $Ma_c = 0$), a liquid solution without solutal Marangoni flows ($C_0 = 0.03$, $Ma_c = 0$) and a liquid solution with solutal Marangoni flows ($C_0 = 0.03$, $Ma_c = 0.54$). For $C_0 = 0.03$, results for z_T and z_M nearly overlap. The parameter values are $\theta_0 = 24.9°$ ($\lambda_c = 0.32$), $\lambda = 0.5$, $\epsilon = 1.7 \times 10^{-3}$, $f_R = 0$, $R_H = 0.45$, $E = 0.265$, $Ma_T = 1.81 \times 10^{-2}$, $K = 9.89$, $\delta = 1.5 \times 10^{-5}$, $\alpha_E = 5 \times 10^{-3}$ and $Pe = 4.3 \times 10^6$.

effects with and without evaporation by including (2.36) in our governing equations. To fully fill the channel and avoid depletion of the reservoir in the absence of evaporation requires at the maximum $f_R = 3/(6 - \pi\epsilon\lambda) \approx 1/2$. Note that if the reservoir is initially overfilled, then the maximum f_R required to avoid reservoir depletion increases (e.g. initial $V_R = 3/2$ requires $f_R = 6/(6 - \pi\epsilon\lambda) \approx 1$). As depicted in figure 8(*d*), for $E = 0$ and $f_R \ll 1/2$ the reservoir size has negligible effect on z_T and z_M and the liquid reaches the end of the channel ($z = 1$). However, when $f_R > 1/2$ a decrease in the total flow distances is observed due to depletion of the reservoir, and further increasing f_R results in a monotonic decrease in z_T and z_M.

In the presence of evaporation ($E > 0$; red lines), the flow distances are significantly reduced due to faster depletion of the reservoir relative to the case where evaporation is absent ($E = 0$; blue lines). We isolate the influence of the reservoir depletion due to evaporation by comparing results for finite-size reservoirs ($f_R > 0$; red lines) with those obtained assuming an infinite reservoir ($f_R = 0$; green lines). Shorter flow distances are observed for all $f_R > 0$ compared with $f_R = 0$, because in the limit of $f_R \to 0$, the evaporative mass flux in the reservoir $\tilde{J}_R$ is non-zero and asymptotically approaches the thin-film limit of $\tilde{J}_R = 1/(2K + 2)$ due to the finite reservoir height $\hat{H}$, while $\tilde{J}_R = 0$ for $f_R = 0$. Therefore, reservoir depletion results in flow termination for all $f_R > 0$ prior to what would be observed for $f_R = 0$. While in this comparison we considered $\lambda = 0.5$ ($\lambda > \lambda_c$), similar trends are seen for $\lambda < \lambda_c$.

5. Results: liquid solutions

Here, we consider the influence of solute-concentration gradients that arise during the flow of an evaporating liquid solution, using 3 wt% aqueous PVA solutions as an example motivated by the experiments of Lade *et al.* (2018). The polymer solution viscosity and surface tension are given by the constitutive equations (2.23*a*) and (2.24), respectively. In this section we chose representative parameter values $R_H = 0.45$, $\Delta\hat{T} = 11$ K, $\hat{H} = 50\,\mu\text{m}$, $\alpha_E = 5 \times 10^{-3}$ and $\epsilon = 1.7 \times 10^{-3}$ (table 1). Two additional dimensionless parameters that arise are the solutal Marangoni number Ma_c and the Péclet number Pe (table 2).

The addition of solute affects both the viscosity and surface tension, so we initially consider their effects separately. In figure 9, we present numerical solutions of the evolution of the finger tip position z_T and meniscus position z_M of a pure solvent, a liquid solution with a constant
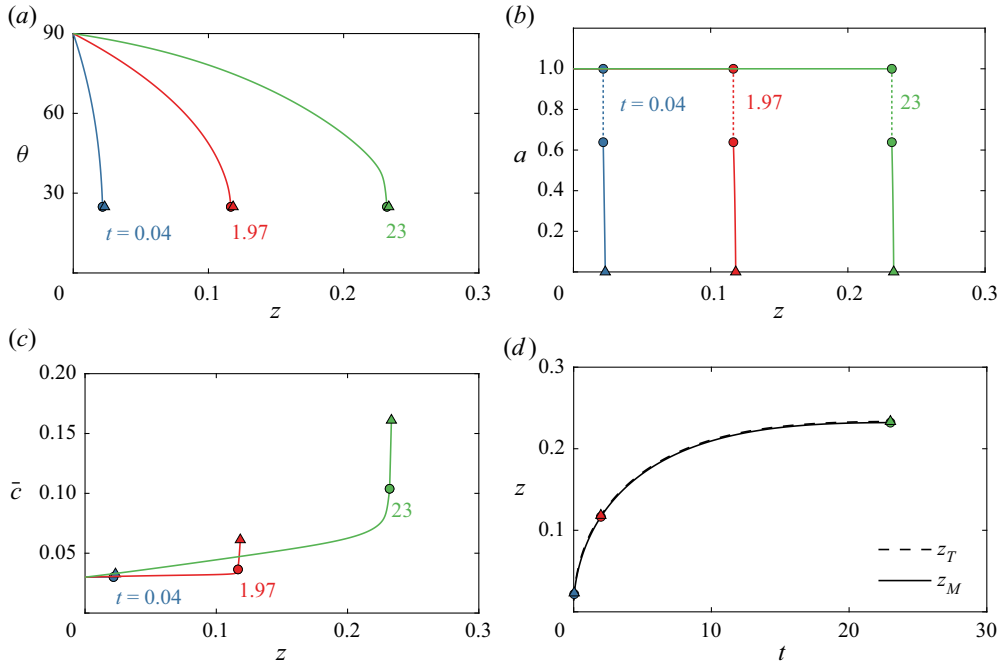
Figure 10. Evolution of (*a*) contact angle on channel sidewall θ, (*b*) liquid height on channel sidewall a, (*c*) cross-sectional-averaged concentration $\bar{c}$ and (*d*) finger tip position z_T and meniscus position z_M. Results for z_T and z_M nearly overlap. The parameter values are $\theta_0 = 24.9°$ ($\lambda_c = 0.32$), $\lambda = 0.5$, $\epsilon = 1.7 \times 10^{-3}$, $f_R = 0$, $C_0 = 0.03$, $R_H = 0.45$, $E = 0.26$, $Ma_T = 1.81 \times 10^{-2}$, $K = 9.89$, $\delta = 1.5 \times 10^{-5}$, $\alpha_E = 5 \times 10^{-3}$, $Ma_c = 0.54$ and $Pe = 4.3 \times 10^6$.

surface tension, and a liquid solution with a concentration-dependent surface tension. Solutions are obtained by solving (2.27) and (2.22) for each regime in figure 1.

Including a concentration-dependent viscosity significantly decreases the finger tip and meniscus positions, and including solutal Marangoni effects further decreases the finger tip and meniscus positions. However, it is evident from figure 9 that the concentration-dependent viscosity is primarily responsible for the change in the finger tip and meniscus evolution for this polymer solution. An increase in the solute concentration near the meniscus and fingers due to solute evaporation causes an increase in the local viscosity which inhibits flow (see figure 10). The axial temperature variations do influence the viscosity when $C_0 > 0$, although their effect is negligible compared with that from the solute concentration variations (see (2.23*a*)). Qualitatively similar results are expected for colloidal suspensions where the viscosity diverges ($M \to \infty$) as the particle concentration approaches the maximum packing fraction. Solutal Marangoni effects are expected to be primarily responsible for the change in the finger tip and meniscus evolution for surfactant solutions, where the presence of surfactants typically does not significantly influence the bulk viscosity (Yiantsios & Higgins 2010).

We present numerical solutions of the contact angle $\theta(z, t)$ and the liquid height $a(z, t)$ on the channel sidewall for $\lambda > \lambda_c$ and $\lambda < \lambda_c$ in figures 10 and 11, respectively. Solutions are obtained by solving (2.27) and (2.22) for each regime in figure 1. For $\lambda > \lambda_c$, the $\theta(z, t)$ and $a(z, t)$ profiles in figures 10(*a*) and 10(*b*) are qualitatively similar for most of the flow domain to those obtained for a pure solvent in figure 5, except in the fingers. This is caused by an increase in solute concentration at the meniscus position and fingers depicted in figure 10(*c*), which locally increases the viscosity and reduces the finger size. This results in the flow being dominated by
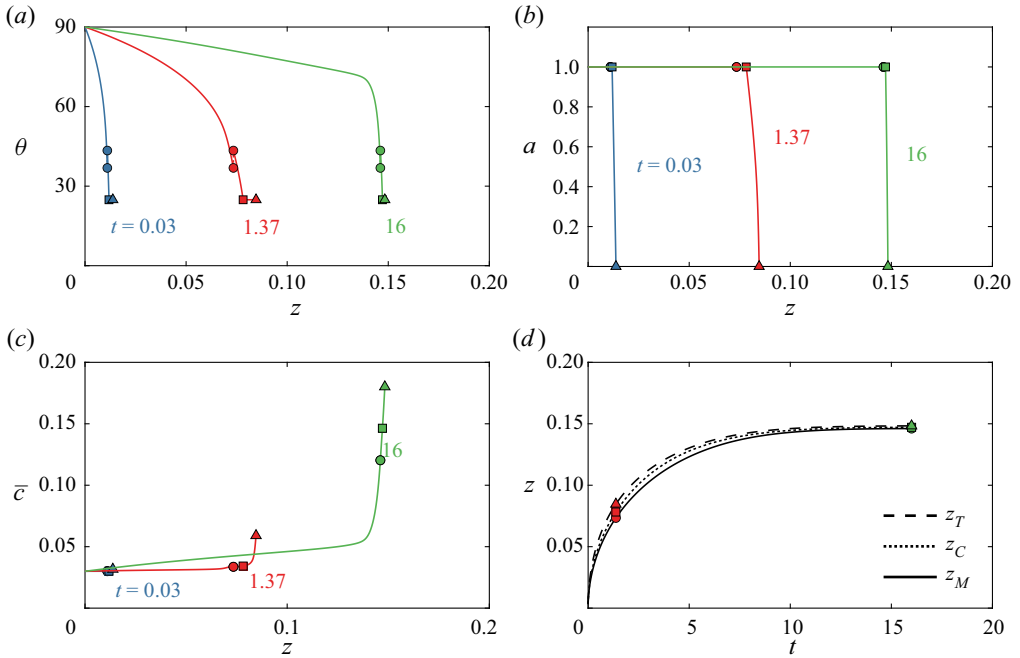
Figure 11. Evolution of (*a*) contact angle on channel sidewall θ, (*b*) liquid height on channel sidewall a, (*c*) cross-sectional-averaged concentration $\bar{c}$ and (*d*) finger tip position z_T, finger depinning position z_C and meniscus position z_M. The parameter values are $\theta_0 = 24.9°$ ($\lambda_c = 0.32$), $\lambda = 0.25$, $\epsilon = 1.7 \times 10^{-3}$, $f_R = 0$, $C_0 = 0.03$, $R_H = 0.45$, $E = 0.265$, $Ma_T = 1.81 \times 10^{-2}$, $K = 9.89$, $\delta = 1.5 \times 10^{-5}$, $\alpha_E = 5 \times 10^{-3}$, $Ma_c = 0.54$ and $Pe = 4.3 \times 10^6$.

the meniscus-deformation regime as is shown in the three-dimensional free-surface profiles in figure 12(*a*), where the finger size is negligible.

Similar to the pure-liquid case, the finger tip position z_T and meniscus position z_M approach an asymptotic plateau seen in figure 10(*d*). However, the underlying cause is quite different. For a pure liquid, a steady state is reached when capillary flow is balanced by evaporation. For a polymer solution, the local increase in viscosity due to solute accumulation at the liquid front is what causes termination of the flow.

For $\lambda < \lambda_c$, qualitative differences are observed between the polymer solution (figure 11) and the pure liquid (figure 6). Like the case where $\lambda > \lambda_c$, the $\theta(z, t)$ and $a(z, t)$ profiles in figures 11(*a*) and 11(*b*) are qualitatively similar for most of the flow domain to those obtained for a pure liquid in figure 6, except in the fingers. The increase in solute concentration near the meniscus position and fingers (figure 11*c*) results in a local increase in viscosity, hindering the flow in the fingers. Similar to $\lambda > \lambda_c$, the finger tip position z_T, finger depinning position z_C, and meniscus position z_M approach an asymptotic plateau (figure 11*d*) due to the local increase in viscosity caused by solute accumulation at the liquid front, which results in flow termination. This local increase in viscosity influences the three-dimensional free-surface profiles in figure 12(*b*), where the finger size is negligible.

We consider the effect of the Péclet number Pe and the solutal Marangoni number Ma_c on the maximum values of z_T, z_C and z_M in figures 13(*a*) and 13(*b*), respectively. The Péclet number controls the ratio of convective to diffusive solute mass transport, where larger Pe signifies weaker solute diffusion. Thus, increasing Pe in figure 13(*a*) leads to a decrease in the maximum values of z_T, z_C and z_M, since increasing Pe (reducing solute diffusion) leads to larger solute concentration gradients near the meniscus and fingers.
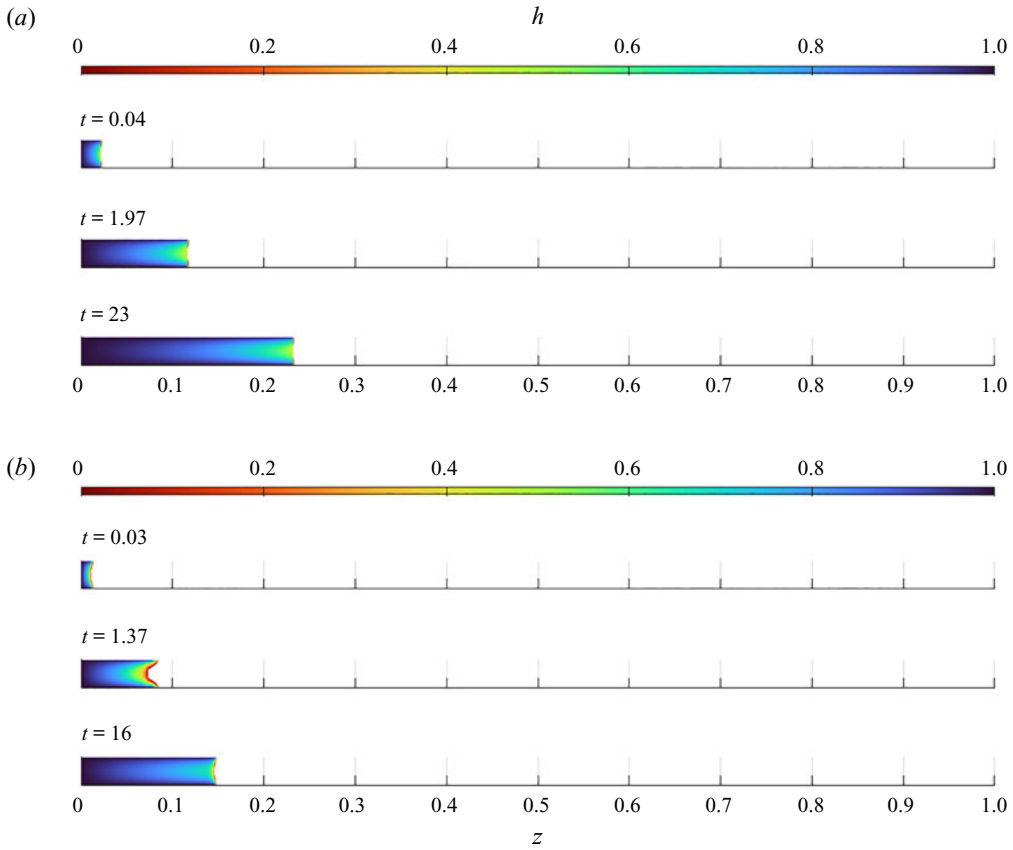
Figure 12. Evolution of liquid height profile h (top view) for (a) $\lambda = 0.5$ and (b) $\lambda = 0.25$. The corresponding parameter values are given in the captions of figures 10 and 11, respectively. Discontinuities in h are caused by discontinuities in θ and a seen in figures 10 and 11.
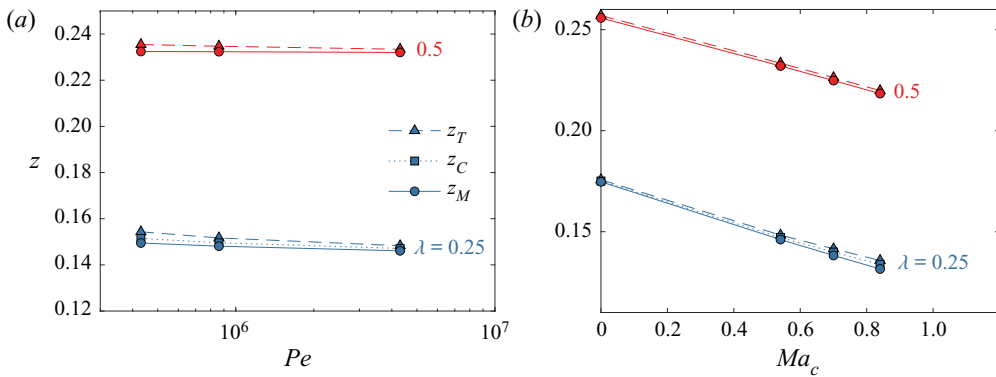

Figure 13. Final finger tip z_T, finger depinning z_C and meniscus position z_M as a function of (a) Péclet number Pe and (b) solutal Marangoni number Ma_c. Unless denoted otherwise, the parameter values are $\theta_0 = 24.9°$ ($\lambda_c = 0.32$), $\epsilon = 1.7 \times 10^{-3}$, $f_R = 0$, $C_0 = 0.03$, $R_H = 0.45$, $E = 0.265$, $Ma_T = 1.81 \times 10^{-2}$, $K = 9.89$, $\delta = 1.5 \times 10^{-5}$, $\alpha_E = 5 \times 10^{-3}$, $Ma_c = 0.54$ and $Pe = 4.3 \times 10^6$.
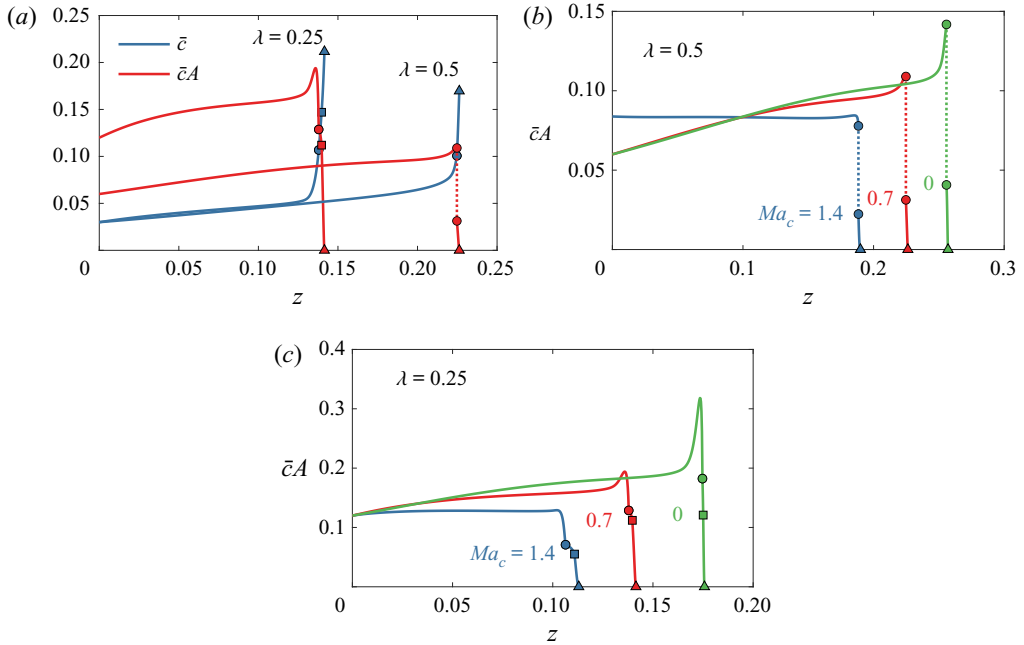
Figure 14. (*a*) Comparison of solute concentration $\bar{c}$ and solute distribution $\bar{c}A$ profiles for different λ at the maximum flow distance. Effect of solutal Marangoni number Ma_c on solute distribution profile $\bar{c}A$ for (*b*) $\lambda = 0.5$ ($\lambda > \lambda_c$) and (*c*) $\lambda = 0.25$ ($\lambda < \lambda_c$). Unless denoted otherwise, the parameter values are $\theta_0 = 24.9°$ ($\lambda_c = 0.32$), $\epsilon = 1.7 \times 10^{-3}$, $f_R = 0$, $R_H = 0.45$, $E = 0.265$, $Ma_c = 0.7$, $Ma_T = 1.81 \times 10^{-2}$, $K = 9.89$, $\delta = 1.5 \times 10^{-5}$, $\alpha_E = 5 \times 10^{-3}$ and $Pe = 4.3 \times 10^6$.

The solutal Marangoni number Ma_c controls the magnitude of the surface-tension-gradient forces caused by solute-concentration gradients. The cross-sectional-averaged concentration $\bar{c}$ increases down the length of the channel (figures 10*c* and 11*c*), causing the surface tension Σ to decrease due to (2.24). Decreasing Σ decreases the magnitude of the capillary-pressure gradients in $\bar{w}_{ca}$ (which drive flow) and increases the magnitude of the solutal Marangoni stresses in $\bar{w}_{cg}$ (which inhibit flow), thus reducing the axial velocity and propagation of the liquid front. Hence, increasing Ma_c in figure 13(*b*) leads to a decrease in the maximum values of z_T, z_C and z_M.

It is important to differentiate between the concentration profiles $\bar{c}$ depicted in figures 10(*c*) and 11(*c*) and the final solute deposition pattern resulting from the solvent evaporation. The reason these can be qualitatively different is because the solute concentration is the ratio between the amount of solute and the amount of solution. Therefore, a high solute concentration can be obtained with a small amount of solute and a small amount of solution. Prior studies on droplets (Deegan *et al.* 2000; Wray *et al.* 2014; Pham & Kumar 2017, 2019) and thin films (Warner, Craster & Matar 2003) have demonstrated that a better measure of the eventual solute deposition pattern is the solute area density $\bar{c}h$. In our system, the solute deposition is characterized by the solute linear density $\bar{c}A$ because our concentration is cross-sectionally averaged, in contrast to the height-averaged concentration considered in droplets and thin films.

In figure 14(*a*) we compare the final concentration $\bar{c}$ from figures 10(*c*) and 11(*c*) with the final solute distribution $\bar{c}A$ for $\lambda > \lambda_c$ and $\lambda < \lambda_c$. There is a significant qualitative difference in the $\bar{c}$ and $\bar{c}A$ profiles. The concentration profiles suggest an accumulation of solute near the meniscus position (circles) and in the fingers (between circles and triangles), for $\lambda > \lambda_c$ and $\lambda < \lambda_c$. However, the distribution profiles demonstrate that the solute accumulates the most before the meniscus position (circles) and the amount of solute in the fingers is significantly less than that
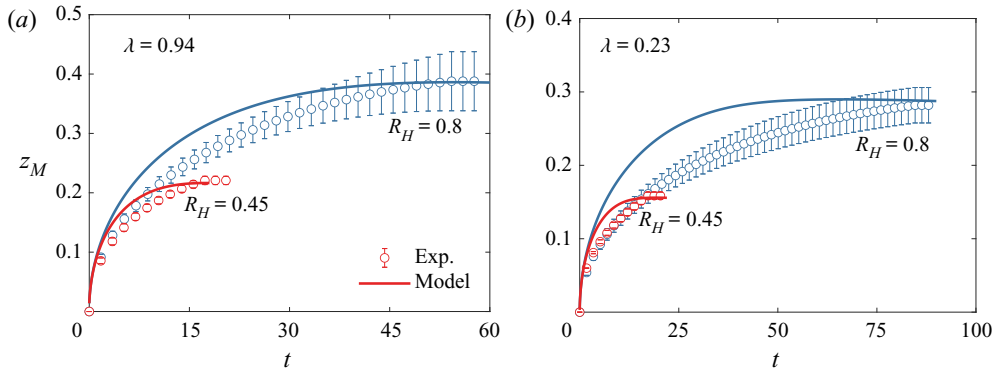
Figure 15. Effect of relative humidity R_H on evolution of meniscus position z_M for (a) $\lambda = 0.94$ and (b) $\lambda = 0.23$. Note that $\lambda_c = 0.32$. Symbols represent experimental results of Lade *et al.* (2018) and solid lines represent lubrication-theory-based model predictions using the accommodation coefficient α_E as a fitting parameter (see table 3). Parameter values are calculated using table 1 and can be found in the supplementary material.

upstream of the meniscus position. These solute distribution profiles are in qualitative agreement with the deposition patterns observed by Lade *et al.* (2018) for capillary flow and evaporation of PVA solutions (see figure 8 in Lade *et al.* 2018).

In figures 14(b) ($\lambda > \lambda_c$) and 14(c) ($\lambda < \lambda_c$) we compare $\bar{c}A$ profiles for different solutal Marangoni numbers Ma_c. In both cases it is observed that the solute accumulation can be reduced significantly by increasing the solutal Marangoni number Ma_c. Increasing Ma_c reduces the axial velocity and propagation of the liquid front as shown in figure 13(b) but also reduces the convection of solute, leading to a more uniform solute deposition pattern. This suggests a trade-off between obtaining longer flow distances and uniform deposition patterns. Additional calculations (not shown here) reveal that solute distribution profiles also tend to become more uniform as the thermal Marangoni number Ma_T increases because the thermal Marangoni stresses drive flow away from the meniscus and fingers (§ 4.2).

6. Comparison with experiments

Kolliopoulos *et al.* (2019) studied capillary flow and evaporation in open rectangular microchannels by extending the Lucas–Washburn model to include effects of concentration-dependent viscosity and uniform evaporation, and compared model predictions with experiments by Lade *et al.* (2018). Evaporative mass flux values used to fit the model to the experiments by Lade *et al.* (2018) were $O(10 - 10^2)$ larger than estimates obtained from the experiments. The discrepancy was attributed to assuming a flat free surface and not accounting for axial concentration gradients in the model.

Here, we account for the effects of evaporation on capillary flow by using the accommodation coefficient α_E as the only fitting parameter to match the predicted final meniscus position z_M to that experimentally observed by Lade *et al.* (2018). (All other parameters are determined using the values in table 1 and can be found in the supplementary material.) The comparison of the meniscus position evolution z_M is depicted in figures 15(a) ($\lambda > \lambda_c$) and 15(b) ($\lambda < \lambda_c$) for different relative humidities R_H. Symbols represent experimental results of Lade *et al.* (2018) and model predictions are shown in solid lines. In general, good agreement is observed between the model predictions and the experimental results. The model predicts that the meniscus position increases at a faster rate than what is observed in the experiments, and that the total flow distance is reached sooner. This is likely due to channel roughness in the experiments that arises due to the fabrication process (Lade *et al.* 2018), which is not accounted for in the model. Xing *et al.* (2020)

R_H	λ	$\bar{J}_{exp}$	$\bar{J}_R$	$\bar{J}_C$	α_E
0.45	0.94	9.9×10^{-2}	8.5×10^{-2}	4.6×10^{-2}	5.0×10^{-3}
0.80	0.94	20.9×10^{-2}	14.1×10^{-2}	8.1×10^{-2}	5.4×10^{-3}
0.45	0.23	9.9×10^{-2}	5.8×10^{-2}	3.2×10^{-2}	3.3×10^{-3}
0.80	0.23	20.9×10^{-2}	9.3×10^{-2}	5.1×10^{-2}	3.3×10^{-3}

Table 3. Dimensionless evaporative mass flux values from experiments $\bar{J}_{exp}$ by Lade *et al.* (2018) for different relative humidities R_H and aspect ratios λ are compared with model predictions of the dimensionless evaporative mass flux values for the reservoir $\bar{J}_R$ and channel $\bar{J}_C$ by using the accommodation coefficient α_E as a fitting parameter.

combined theory and experiment to demonstrate that channel roughness can cause significant inhibition of capillary flow in U-shaped channels in the absence of evaporation. However, the channel roughness in the experiments by Lade *et al.* (2018) was likely not as pronounced as that in the study by Xing *et al.* (2020) based on micrographs of the channels and the channel fabrication methods reported in each study.

Lade *et al.* (2018) obtained estimates for the evaporative mass flux $\bar{J}_{exp}$ in the capillary-flow experiments by measuring the mass loss in a cylindrical dish under the same experimental conditions. We note that the cylindrical dish ($\hat{R} = 2.875$ mm, $\hat{H} = 1.25$ mm) is considerably larger than the channel reservoir ($\hat{R} = 1.5$ mm, $\hat{H} = 46.8\,\mu$m) used in the capillary-flow experiments. We compare these estimates for $\bar{J}_{exp}$ with the time-averaged mass flux for the reservoir $\bar{J}_R$ and the channel $\bar{J}_C$, which are given by

$$\bar{J}_R = \frac{1}{t_F} \int_0^{t_F} \frac{\tilde{J}_R}{S_R}\, \mathrm{d}t, \tag{6.1a}$$

$$\bar{J}_C = \frac{1}{t_F} \int_0^{t_F} \left[\frac{1}{z_T} \int_0^{z_T} \frac{\tilde{J}}{S}\, \mathrm{d}z \right] \mathrm{d}t, \tag{6.1b}$$

where t_F is the total flow time.

This comparison is given in table 3 for different relative humidities R_H and different channel aspect ratios λ, along with the values of α_E used in figure 15. Table 3 illustrates that the flux values for both the reservoir $\bar{J}_R$ and channel $\bar{J}_C$ are comparable to the experimentally measured values $\bar{J}_{exp}$, suggesting that the kinetically limited evaporation model provides physically reasonable predictions.

As discussed previously, the accommodation coefficients used in the literature vary over several orders of magnitude from $O(10^{-6})$ to $O(1)$ (Marek & Straub 2001; Murisic & Kondic 2011; Persad & Ward 2016), with $\alpha_E = 1$ corresponding to no barrier to phase change and $\alpha_E = 0$ corresponding to no phase change. In addition, interfaces that are considered contaminated typically have $\alpha_E \ll 1$ (Cazabat & Guéna 2010; Murisic & Kondic 2011), since contaminants likely hinder the phase change of the volatile species. The α_E values in table 3 are within the range of values used in the literature and their order of magnitude seems reasonable since PVA at the liquid–air interface may act like a contaminant.

In figure 15 and table 3 we account for thermal and solutal Marangoni flows which influence the flow dynamics (figures 8c and 13b). The channel-to-reservoir volume ratio in these experiments is $f_R = 0.21$ ($\lambda = 0.94$) and $f_R = 0.85$ ($\lambda = 0.23$), so reservoir depletion significantly influences the maximum meniscus position z_M (figure 8d). Fitting the model to experiments by solely accounting for the concentration-dependent viscosity and assuming the surface tension is constant (neglecting Marangoni stresses) and an infinite reservoir size ($f_R = 0$)

yields accommodation coefficients and mass flux values having the same order of magnitude as those listed in table 3. The sensitivity of the results to the value of α_E is characterized in the supplementary material. This indicates that the dominant effect inhibiting the flow is the concentration-dependent viscosity, which increases near the meniscus position and fingers due to the increase in solute concentration caused by solvent evaporation (figure 9).

7. Conclusions

In this work we develop a lubrication-theory-based model to examine capillary flow of evaporating liquid solutions in open rectangular microchannels. In addition to describing the complex free-surface morphology, the model accounts for non-uniform solvent evaporation, Marangoni flows due to gradients in solute concentration and temperature, and the effects of a finite-size reservoir connected to the microchannel. These latter factors were not considered by Kolliopoulos *et al.* (2021) who focused on non-volatile liquids, and by Kolliopoulos *et al.* (2019) where very simplified descriptions of fluid flow and evaporation were employed.

Thermal effects on the flow dynamics are elucidated by considering a pure solvent. The flow is shown to asymptotically approach a steady state where capillary flow is balanced by evaporation when the reservoir is infinite. The dependence of the maximum finger tip, finger depinning, and meniscus positions at steady state on the channel aspect ratio λ, evaporation number E and thermal Marangoni number Ma_T is presented. For finite-size reservoirs, a steady state is not obtained and the critical reservoir size is identified for which reservoir depletion results in reduced maximum flow distances compared with the infinite reservoir case.

Solute-concentration effects on the flow dynamics are examined by considering aqueous PVA solutions. Rather than approaching a steady state, the flow terminates due to a local increase in viscosity caused by an increase in solute concentration at the liquid front. As a consequence, fingers are suppressed. Notably, stronger Marangoni flows are found to lead to more uniform solute deposition patterns, which is important for applications involving printed electronics, where uniform solute deposition is needed for electronic devices to function well.

Finally, model predictions of the meniscus position evolution are compared with capillary-flow experiments conducted by Lade *et al.* (2018). Results demonstrate that the lubrication-theory-based model captures the evolution of the meniscus position seen in experiments, and the evaporative mass flux values obtained from the kinetically limited model are comparable to the experimental estimates of Lade *et al.* (2018).

Results from our lubrication-theory-based model reveal significant qualitative differences in capillary flow of evaporating pure solvents and liquid solutions, and advance fundamental physical understanding of the flow dynamics. This understanding is vital for improving and optimizing a number of technological applications such as lab-on-a-chip devices, where evaporation is generally undesirable, as well as evaporative lithography and printed electronics manufacturing, where evaporation is exploited. The results of the present work provide a foundation for designing additional experiments to more thoroughly test the model predictions, as well as for conducting direct numerical simulations to explore phenomena and parameter regimes beyond the scope of the present model.

Author ORCIDs.

Ⓘ Panayiotis Kolliopoulos https://orcid.org/0000-0003-3774-7063;

Ⓘ Krystopher S. Jochem https://orcid.org/0000-0003-0860-2316;

Ⓘ Lorraine F. Francis https://orcid.org/0000-0003-2516-2957;

Ⓘ Satish Kumar https://orcid.org/0000-0003-0829-6355.

REFERENCES

AJAEV, V.S. 2005 Spreading of thin volatile liquid droplets on uniformly heated surfaces. *J. Fluid Mech.* **528**, 279–296.

AJAEV, V.S. & HOMSY, G.M. 2001 Steady vapor bubbles in rectangular microchannels. *J. Colloid Interface Sci.* **240** (1), 259–271.

AYYASWAMY, P.S., CATTON, I. & EDWARDS, D.K. 1974 Capillary flow in triangular grooves. *J. Appl. Mech.* **41** (2), 332–336.

BERTHIER, J., GOSSELIN, D. & BERTHIER, E. 2015 A generalization of the Lucas–Washburn–Rideal law to composite microchannels of arbitrary cross section. *Microfluid Nanofluid* **19** (3), 497–507.

BOSANQUET, C.H. 1923 LV. On the flow of liquids into capillary tubes. *Phil. Mag.* **45** (267), 525–531.

BURELBACH, J.P., BANKOFF, S.G. & DAVIS, S.H. 1988 Nonlinear stability of evaporating condensing liquid-films. *J. Fluid Mech.* **195**, 463–494.

CAO, M., JOCHEM, K.S., HYUN, W.-J., FRANCIS, L.F. & FRISBIE, C.D. 2018 Self-aligned inkjet printing of resistors and low-pass resistor – capacitor filters on roll-to-roll imprinted plastics with resistances ranging from 10 to 10^6 Ω. *Flex. Print. Electron.* **3**, 045003.

CAZABAT, A.-M. & GUÉNA, G. 2010 Evaporation of macroscopic sessile droplets. *Soft Matt.* **6** (12), 2591–2612.

CHEN, T. 2014 Capillary force-driven fluid flow of a wetting liquid in open grooves with different sizes. In *Fourteenth Intersociety Conference on Thermal and Thermomechanical Phenomena in Electronic Systems (ITherm)*, pp. 388–396. IEEE.

CONCUS, P. & FINN, R. 1969 On the behaviour of a capillary surface in a wedge. *Proc. Natl Acad. Sci. USA* **63** (2), 292–299.

CRASTER, R.V., MATAR, O.K. & SEFIANE, K. 2009 Pinning, retraction, and terracing of evaporating droplets containing nanoparticles. *Langmuir* **25** (6), 3601–3609.

DEEGAN, R.D., BAKAJIN, O., DUPONT, T.F., HUBER, G., NAGEL, S.R. & WITTEN, T.A. 2000 Contact line deposits in an evaporating drop. *Phys. Rev.* E **62** (1), 756–765.

FAGHRI, A. 1995 *Heat Pipe Science and Technology*. Global Digital Press.

FAGHRI, A. 2012 Review and advances in heat pipe science and technology. *Trans. ASME J. Heat Transfer* **134** (12), 1–18.

GAMBARYAN-ROISMAN, T. 2019 Simultaneous imbibition and evaporation of liquids on grooved substrates. *Interfacial Phenom. Heat Transfer* **7** (3), 239–253.

GRAMLICH, C.M., KALLIADASIS, S., HOMSY, G.M. & MESSER, C. 2002 Optimal leveling of flow over one-dimensional topography by Marangoni stresses. *Phys. Fluids* **14** (6), 1841–1850.

GURUMURTHY, V.T., ROISMAN, I.V., TROPEA, C. & GAROFF, S. 2018 Spontaneous rise in open rectangular channels under gravity. *J. Colloid Interface Sci.* **527**, 151–158.

JENSEN, O.E. & GROTBERG, J.B. 1993 The spreading of heat or soluble surfactant along a thin liquid film. *Phys. Fluids* **5**, 58–68.

JOCHEM, K.S., KOLLIOPOULOS, P., BIDOKY, F.Z., WANG, Y., KUMAR, S., FRISBIE, C.D. & FRANCIS, L.F. 2020 Self-aligned capillarity-assisted printing of high aspect ratio flexible metal conductors: optimizing ink flow, plating, and mechanical adhesion. *Ind. Engng Chem. Res.* **59** (51), 22107–22122.

JOCHEM, K.S., SUSZYNSKI, W.J., FRISBIE, C.D. & FRANCIS, L.F. 2018 High-resolution, high-aspect-ratio printed and plated metal conductors utilizing roll-to-roll microscale UV imprinting with prototype imprinting stamps. *Ind. Engng Chem. Res.* **57** (48), 16335–16346.

KHRUSTALEV, D. & FAGHRI, A. 1994 Thermal analysis of a micro heat pipe. *Trans. ASME J. Heat Transfer* **116** (1), 189–198.

KOLLIOPOULOS, P., JOCHEM, K.S., JOHNSON, D., SUSZYNSKI, W.J., FRANCIS, L.F. & KUMAR, S. 2021 Capillary-flow dynamics in open rectangular microchannels. *J. Fluid Mech.* **911**, A32.

KOLLIOPOULOS, P., JOCHEM, K.S., LADE, R.K., JR., FRANCIS, L.F & KUMAR, S. 2019 Capillary flow with evaporation in open rectangular microchannels. *Langmuir* **35** (24), 8131–8143.

LADE, R.K., JR., JOCHEM, K.S., MACOSKO, C.W. & FRANCIS, L.F. 2018 Capillary coatings: flow and drying dynamics in open microchannels. *Langmuir* **34** (26), 7624–7639.

LAM, V.T. & BENSON, G.C. 1970 Surface tensions of binary liquid systems. I. Mixtures of nonelectrolytes. *Can. J. Chem.* **48** (24), 3773–3781.

LENORMAND, R. & ZARCONE, C. 1984 Role of roughness and edges during imbibition in square capillaries. In *SPE Annual Technical Conference and Exhibition*, pp. 1–17. Society of Petroleum Engineers.

LIU, H., SUN, S., WU, R., WEI, B. & HOU, J. 2021 Pore-scale modeling of spontaneous imbibition in porous media using the lattice Boltzmann method. *Water Resour. Res.* **57** (6), e2020WR029219.

LONE, S., ZHANG, J.M., VAKARELSKI, I.U., LI, E.Q. & THORODDSEN, S.T. 2017 Evaporative lithography in open microfluidic channel networks. *Langmuir* **33** (11), 2861–2871.

LUCAS, R. 1918 Ueber das Zeitgesetz des kapillaren Aufstiegs von Flüssigkeiten. *Kolloid Z.* **23**, 15–22.

MAHAJAN, A., HYUN, W.-J., WALKER, S.B., ROJAS, G.A., CHOI, J.-H., LEWIS, J.A., FRANCIS, L.F. & FRISBIE, C.D. 2015 A self-aligned strategy for printed electronics: exploiting capillary flow on microstructured plastic surfaces. *Adv. Electron. Mater.* **1** (9), 1500137.

MANN, J.A., ROMERO, L.A., RYE, R.R. & YOST, F.G. 1995 Flow of simple liquids down narrow V grooves. *Phys. Rev.* E **52** (4), 3967–3972.

MAREK, R. & STRAUB, J. 2001 Analysis of the evaporation coefficient and the condensation coefficient of water. *Intl J. Heat Mass Transfer* **44** (1), 39–53.

MARKOS, M., AJAEV, V.S. & HOMSY, G.M. 2006 Steady flow and evaporation of a volatile liquid in a wedge. *Phys. Fluids* **18** (9), 092102.

MOOSMAN, S. & HOMSY, G.M. 1980 Evaporating menisci of wetting fluids. *J. Colloid Interface Sci.* **73** (1), 212–223.

MURISIC, N. & KONDIC, L. 2011 On evaporation of sessile drops with moving contact lines. *J. Fluid Mech.* **679**, 219–246.

NARAYANAMURTHY, V., JEROISH, Z.E., BHUVANESHWARI, K.S., BAYAT, P., PREMKUMAR, R., SAMSURI, F. & YUSOFF, M.M. 2020 Advances in passively driven microfluidics and lab-on-chip devices: A comprehensive literature review and patent analysis. *RSC Adv.* **10** (20), 11652–11680.

NILSON, R.H., TCHIKANDA, S.W., GRIFFITHS, S.K. & MARTINEZ, M.J. 2006 Steady evaporating flow in rectangular microchannels. *Intl J. Heat Mass Transfer* **49** (9–10), 1603–1618.

OLANREWAJU, A., BEAUGRAND, M., YAFIA, M. & JUNCKER, D. 2018 Capillary microfluidics in microchannels: from microfluidic networks to capillaric circuits. *Lab Chip* **18** (16), 2323–2347.

OUALI, F.F., MCHALE, G., JAVED, H., TRABI, C., SHIRTCLIFFE, N.J. & NEWTON, M.I. 2013 Wetting considerations in capillary rise and imbibition in closed square tubes and open rectangular cross-section channels. *Microfluid Nanofluid* **15** (3), 309–326.

PATTON, T.C. 1964 *Paint Flow and Pigment Dispersion*, 2nd edn. John Wiley & Sons.

PERSAD, A.H. & WARD, C.A. 2016 Expressions for the evaporation and condensation coefficients in the Hertz-Knudsen relation. *Chem. Rev.* **116** (14), 7727–7767.

PETERSON, G.P. & MA, H.B. 1996 Theoretical analysis of the maximum heat transport in triangular grooves: A study of idealized micro heat pipes. *Trans. ASME J. Heat Transfer* **118** (3), 731–739.

PHAM, T., CHENG, X. & KUMAR, S. 2017 Drying of multicomponent thin films on substrates with topography. *J. Polym. Sci. Pol. Phys.* **55**, 1681–1691.

PHAM, T. & KUMAR, S. 2017 Drying of droplets of colloidal suspensions on rough substrates. *Langmuir* **33**, 10061–10076.

PHAM, T. & KUMAR, S. 2019 Imbibition and evaporation of droplets of colloidal suspensions on permeable substrates. *Phys. Rev. Fluids* **4** (3), 034004.

PLESSET, M.S. & PROSPERETTI, A. 1976 Flow of vapour in a liquid enclosure. *J. Fluid Mech.* **78** (3), 433–444.

POPESCU, M.N., RALSTON, J. & SEDEV, R. 2008 Capillary rise with velocity-dependent dynamic contact angle. *Langmuir* **24** (21), 12710–12716.

QUÉRÉ, D. 1997 Inertial capillarity. *Europhys. Lett.* **39** (5), 533–538.

RANSOHOFF, T.C. & RADKE, C.J. 1988 Laminar flow of a wetting liquid along the corners of a predominantly gas-occupied noncircular pore. *J. Colloid Interface Sci.* **121** (2), 392–401.

RIDEAL, E.K. 1922 On the flow of liquids under capillary pressure. *Phil. Mag.* **44** (264), 1152–1159.

ROMERO, L.A. & YOST, F.G. 1996 Flow in an open channel capillary. *J. Fluid Mech.* **322**, 109–129.

RYE, R.R., MANN, J.A. & YOST, F.G. 1996 The flow of liquids in surface grooves. *Langmuir* **12** (2), 555–565.

RYE, R.R., YOST, F.G. & O'TOOLE, E.J. 1998 Capillary flow in irregular surface grooves. *Langmuir* **14** (14), 3937–3943.

SEFIANE, K. & WARD, C.A. 2007 Recent advances on thermocapillary flows and interfacial conditions during the evaporation of liquids. *Adv. Colloid Interface Sci.* **134-135**, 201–223.

SIEBOLD, A., NARDIN, M., SCHULTZ, J., WALLISER, A. & OPPLIGER, M. 2000 Effect of dynamic contact angle on capillary rise phenomena. *Colloids Surf.* A **161** (1), 81–87.

SOWERS, T.W., SARKAR, R., PRAMEELA, S.E., IZADI, E. & RAJAGOPALAN, J. 2016 Capillary driven flow of polydimethylsiloxane in open rectangular microchannels. *Soft Matt.* **12** (26), 5818–5823.

SUMAN, B. & HODA, N. 2005 Effect of variations in thermophysical properties and design parameters on the performance of a V-shaped micro grooved heat pipe. *Intl J. Heat Mass Transfer* **48**, 2090–2101.

TCHIKANDA, S.W., NILSON, R.H. & GRIFFITHS, S.K. 2004 Modeling of pressure and shear-driven flows in open rectangular microchannels. *Intl J. Heat Mass Transfer* **47** (3), 527–538.

WARNER, M.R.E., CRASTER, R.V. & MATAR, O.K. 2003 Surface patterning via evaporation of ultrathin films containing nanoparticles. *J. Colloid Interface Sci.* **267** (1), 92–110.

WASHBURN, E.W. 1921 The dynamics of capillary flow. *Phys. Rev.* **17** (3), 273–283.

WEISLOGEL, M.M. 2012 Compound capillary rise. *J. Fluid Mech.* **709**, 622–647.

WEISLOGEL, M.M. & LICHTER, S. 1998 Capillary flow in an interior corner. *J. Fluid Mech.* **373**, 349–378.

WEISLOGEL, M.M. & NARDIN, C.L. 2005 Capillary driven flow along interior corners formed by planar walls of varying wettability. *Microgravity Sci. Technol.* **17** (3), 45–55.

WHITE, N.C. & TROIAN, S.M. 2019 Why capillary flows in slender triangular grooves are so stable against disturbances. *Phys. Rev. Fluids* **4** (5), 054003.

WRAY, A.W., PAPAGEORGIOU, D.T., CRASTER, R.V., SEFIANE, K. & MATAR, O.K. 2014 Electrostatic suppression of the "Coffee stain effect". *Langmuir* **30** (20), 5849–5858.

XIA, Z.Z., YANG, G.Z. & WANG, R.Z. 2019 Capillary-assisted flow and evaporation inside circumferential rectangular micro groove. *Intl J. Heat Mass Transfer* **52** (3–4), 952–961.

XING, H., CHENG, J. & ZHOU, C. 2020 Effect of gradient wettability on capillary imbibition in open semicircular copper channel. *Phys. Fluids* **32** (11), 112004.

YANG, L. & HOMSY, G.M. 2006 Steady three-dimensional thermocapillary flows and dryout inside a V-shaped wedge. *Phys. Fluids* **18** (4), 042107.

YANG, D., KRASOWSKA, M., PRIEST, C., POPESCU, M.N. & RALSTON, J. 2011 Dynamics of capillary-driven flow in open microchannels. *J. Phys. Chem.* C **115** (38), 18761–18769.

YIANTSIOS, S.G. & HIGGINS, B.G. 2010 A mechanism of Marangoni instability in evaporating thin liquid films due to soluble surfactant. *Phys. Fluids* **22** (2), 022102.

YOST, F.G., RYE, R.R. & MANN, J.A. 1997 Solder wetting kinetics in narrow V-grooves. *Acta Mater.* **45** (12), 5337–5345.